Biophysical *Journal*
Article

Biophysical Society

Phosphofructokinase relocalizes into subcellular compartments with liquid-like properties in vivo

SoRi Jang,[1] Zhao Xuan,[1] Ross C. Lagoy,[2] Louise M. Jawerth,[3] Ian J. Gonzalez,[1] Milind Singh,[1] Shavanie Prashad,[1] Hee Soo Kim,[1] Avinash Patel,[3] Dirk R. Albrecht,[2] Anthony A. Hyman,[3] and Daniel A. Colón-Ramos[1,4,*]

[1]Department of Neuroscience and Department of Cell Biology, Yale University School of Medicine, New Haven, Connecticut; [2]Department of Biomedical Engineering and Department of Biology and Biotechnology, Worcester Polytechnic Institute, Worcester, Massachusetts; [3]Max Planck Institute of Molecular Cell Biology and Genetics, Dresden, Germany; and [4]Instituto de Neurobiología, Universidad de Puerto Rico, San Juan, Puerto Rico

ABSTRACT Although much is known about the biochemical regulation of glycolytic enzymes, less is understood about how they are organized inside cells. We systematically examine the dynamic subcellular localization of glycolytic protein phosphofructokinase-1/PFK-1.1 in *Caenorhabditis elegans*. We determine that endogenous PFK-1.1 localizes to subcellular compartments in vivo. In neurons, PFK-1.1 forms phase-separated condensates near synapses in response to energy stress from transient hypoxia. Restoring animals to normoxic conditions results in cytosolic dispersion of PFK-1.1. PFK-1.1 condensates exhibit liquid-like properties, including spheroid shapes due to surface tension, fluidity due to deformations, and fast internal molecular rearrangements. Heterologous self-association domain cryptochrome 2 promotes formation of PFK-1.1 condensates and recruitment of aldolase/ALDO-1. PFK-1.1 condensates do not correspond to stress granules and might represent novel metabolic subcompartments. Our studies indicate that glycolytic protein PFK-1.1 can dynamically form condensates in vivo.

SIGNIFICANCE Our study demonstrates that glycolytic proteins can dynamically relocalize in vivo into liquid-like compartments. The study provides a biophysical characterization of the properties of these subcellular compartments in vivo. These biophysical properties might be conserved to organize local metabolism in cells.

INTRODUCTION

Cells are internally organized through compartmentalization. Cellular compartments can delineate areas and locally concentrate molecules of a pathway (1). Although most of our cell biological understanding of compartmentalization is derived from the concept of membrane-bound organelles, an increasing body of work has revealed the existence of membraneless organelles—structures such as the nucleolus, germ granules, and Cajal bodies, which lack physical barriers like lipid membranes but can still self-organize into biomolecular condensates (2,3). An important question in cell biology has become which cytoplasmic processes are organized into these membraneless organelles.

Glycolysis is a metabolic pathway that consists of 10 enzymatic steps. Unlike oxidative phosphorylation, which is housed within the membrane-bound mitochondrion, glycolytic enzymes are soluble proteins in the cytosol for most eukaryotic cells. Early biochemical studies using rat muscle and brain extracts demonstrated that glycolytic proteins interchange between soluble and particulate states depending on different metabolites or hypoxic conditions, suggestive of transient interactions that could result in the subcellular organization of glycolysis (4–9). Studies in red blood cells, which lack mitochondria, suggest that glycolytic proteins compartmentalize near the plasma membrane and that their subcellular organization is important for the regulation of cellular cation pumps (10–12). Immunohistochemical studies on isolated *Drosophila* flight muscle revealed a distinct pattern of colocalization of glycolytic protein isoforms to muscle sarcomeres (13) and vertebrate endothelial cells display enrichment of

Submitted May 28, 2020, and accepted for publication August 5, 2020.

*Correspondence: daniel.colon-ramos@yale.edu

Avinash Patel's present address is Dewpoint Therapeutics GmbH, Dresden, Germany.

Editor: Anne Kenworthy.

https://doi.org/10.1016/j.bpj.2020.08.002

glycolytic proteins to lamellipodia and filopodia, where mitochondria are mostly absent (14). Together, these studies and others suggest that glycolytic proteins could be compartmentalized in specific tissues (15,16). Yet, the notion of a subcellular organization for glycolytic proteins has remained controversial, largely because of the lack of studies examining the dynamic distribution of these enzymes in vivo (17,18).

We recently reported that in *Caenorhabditis elegans* neurons, glycolytic proteins dynamically relocalize near synapses upon energy stress induced by transient hypoxia (19). Glycolytic enzymes were also shown to colocalize into subcellular compartments termed "G-bodies" in yeast (20) and in mammalian tissue culture cells (16). A human isoform of phosphofructokinase (PFK) was shown to assemble into tetramers that oligomerize into higher-ordered filamentous structures in vitro and to dynamically compartmentalize in tissue culture cells in response to specific metabolites (21). Together, these studies indicate that in living cells, glycolytic proteins are not simply diffusely distributed in the cytosol, and suggest the existence of regulatory mechanisms that organize glycolytic proteins in vivo. The purported organization of glycolytic proteins in vivo could have important consequences for the subcellular regulation of this metabolic pathway (15,22,23) and its enzymatic activity (24). How proteins of the glycolytic pathway are subcellularly organized and how their localization is regulated are key questions that remain to be answered.

To examine these questions, we developed a hybrid microfluidic-hydrogel device for use with *C. elegans* to systematically examine and quantify the dynamic subcellular localization of glycolytic proteins in vivo. We focused our study on the rate-limiting enzyme of glycolysis, phosphofructokinase-1/PFK-1.1, and performed high-resolution in vivo imaging of its subcellular localization while precisely and dynamically controlling oxygen levels to transiently inhibit oxidative phosphorylation and induce acute energy stress. Using this system, we observed that in cells in which PFK-1.1 is diffusely localized in the cytosol, such as neurons, the enzyme can dynamically relocalize into biomolecular condensates in response to transient energy stress. Upon return to normoxic conditions, PFK-1.1 dispersed in the cytosol. We further determined that PFK-1.1 condensates exhibit liquid-like properties and that their molecular dynamics, including its viscosity and biophysical properties, change with prolonged hypoxic conditions. We observe that PFK-1.1 and ALDO-1 genetically interact to recruit each other into condensates, indicative of a self-association event that drives a feed-forward loop to recruit glycolytic proteins into condensates. Together, our studies demonstrate that the glycolytic proteins such as PFK-1.1 and ALDO-1 can dynamically compartmentalize in vivo in response to acute energy stress as phase-separated condensates.

MATERIALS AND METHODS

C. elegans strains and transgenic lines

C. elegans were maintained at 20°C using OP50 *Escherichia coli* as a food source as previously described (25). CRY2 expression clone carrying transgenic lines were kept separately in the dark in the same 20°C incubator. *C. elegans* N2 Bristol strain was used as the wild-type. The following mutant strains were received from Shohei Mitani (Tokyo Women's Medical University, Tokyo, Japan): *aldo-1(tm5782)* and *pfk-1.1(tm5741)*. The other strain used in this study is *pfk-1.1(ola72)*. See Supporting materials and methods for details.

Hybrid microfluidic-hydrogel device setup and calibration

A reusable microfluidic polydimethylsiloxane (PDMS) device was fabricated to deliver gases through a channel adjacent to immobilized animals, following protocols as previously described (26). A 50 μm, oxygen-permeable PDMS membrane was permanently bonded using air plasma to create an enclosed arena for gas flow, and the opposite side of the device was permanently bonded to a glass slide for structural integrity. Animals were kept stationary during high-resolution imaging and exposure to shifting gas concentrations at the membrane surface by hydrogel immobilization (27). The gas device was carefully centered and lowered on top of the hydrogel assembly and clamped into a P2 series holder (Warner Instruments, Hamden, CT) to complete the closed system. Lastly, microfluidic tubing and components were connected to a nitrogen tank set to ~1–10 psi using a low-pressure regulator. To generate hypoxic conditions in the hydrogel, nitrogen flow was delivered continuously through the device assembly and confirmed by observing bubbles in a waste beaker filled with water connected with tubing to the device outlet. To generate normoxic conditions in the hydrogel, the nitrogen tank was turned off and the inlet tubing was immediately disconnected at the tank. Note that in addition to the 0% oxygen condition, we also repeated the hypoxic experiments using an 8% oxygen condition in the same setup and obtained similar results (data not shown). *C. elegans* can survive anoxic condition for a whole day (28), and for our hypoxic experiments, which ranged from minutes to an hour, the animals were rescued and shown to be viable post-transient hypoxia. For complete details on the hybrid microfluidic-hydrogel device setup and calibration, see Supporting materials and methods.

Fluorescence recovery after photobleaching of PFK-1.1

For fluorescence recovery after photobleaching (FRAP), a 60 CFI Plan Apo VC (Nikon, Tokyo, Japan), numerical aperture 1.4, oil-immersion objective on an UltraView Vox spinning-disk confocal microscope (PerkinElmer Life and Analytical Sciences, Waltham, MA) and Volocity FRAP Plugin were used. To calibrate the FRAP Plugin, steps laid out in the Volocity User Manual (September 2011 edition), "Calibrating the Photokinesis Accessory," were followed.

For a full FRAP, z-stack images covering the entire volume of the neurite were acquired. A small, circular region, approximately the size of the PFK-1.1 punctum, was used to bleach the entire PFK-1.1 punctum. Recovery images were acquired every 20 s. In ImageJ, acquired images were max projected. Images that passed the following three criteria were used for the analysis: 1) the fluorescence of the PFK-1.1 punctum was not saturated before photobleaching, 2) the punctum was photobleached to at least 80%, and 3) the neurite did not go out of focus during the image acquisition. For the fluorescence recovery calculations, a small region of interest (ROI) was drawn around the bleached punctum to measure its mean fluorescence. The mean fluorescence was then multiplied by the area of the ROI for total fluorescence. The same ROI was used to calculate a background fluorescence level. Background fluorescence was then subtracted from the total fluorescence for each time point. This calculated value was then normalized to the range of

prebleach value as 1 and postbleach value as 0 and plotted against time. In comparing the fluorescence recovery at different time points, *p*-values were calculated using the Mann-Whitney *U*-test.

For a partial FRAP, a small circular ROI was made and used for photobleaching: 17 (w, 2.05 μm) $\times$ 14 (h, 1.69 μm) $\times$ 1 (d, 1 μm) dimension. For consistency, the same dimension was kept constant for all FRAP experiments. This ROI was placed just slightly overlapping with the PFK-1.1::EGFP punctum to cause partial bleaching but not full bleaching of the entire punctum. Single-plane images were acquired at maximum speed, resulting in ~0.1 s intervals for postbleached images. Partial FRAP time-lapse images were analyzed in two ways: 1) kymograph to visualize the fluorescence recovery and 2) to individually calculate the fluorescence change in the bleached and unbleached regions. For calculating the fluorescence change, a small ROI was drawn within the bleached and unbleached regions, and fluorescence was measured throughout time. Kymograph analysis was also performed using ImageJ.

Viscosity estimation from partial FRAP

To understand the diffusion dynamics of PFK-1.1, we used partial photobleaching of PFK-1.1::EGFP in soluble state and in a condensate form. Because PFK-1.1 condensates were slightly bigger in the neuronal cell bodies, partial photobleaching and measurement of fluorescence recovery were conducted on PFK-1.1 found in the neuronal cell bodies. For the normoxia condition, diffuse PFK-1.1 were photobleached and recovery measured. For transient hypoxia condition, PFK-1.1 condensates were induced with nitrogen gas for 10–20 min using the hybrid microfluidic-hydrogel device and then partially photobleached. From there, fluorescence recovery curves were obtained using the FRAP analysis plugin developed by Robert Haase of the Scientific Computing Facility at Max Planck Institute of Molecular Cell Biology and Genetics. In summary, the measured signal was corrected using a reference point, and all values were normalized to the corrected signal at photobleaching as 0 for both the fluorescence recovery and time. The plotted FRAP data were then fitted to an exponential equation, $y = 1 - ae^{-bt} - c$. Here, t is time in seconds; y is the normalized fluorescence recovery fraction; and a, b, and c are variables, where a and b are positive values and $a + c$ is close to 1. From this exponential curve fitting, half time (τ, in seconds) was calculated and related to the diffusion coefficient (D) via a diffusion equation in a two-dimensional space, $r^2 = 4D\tau$. Using the fluorescence recovery, viscosity was approximated as previously described (29). Briefly, the Stokes-Einstein relationship $D = (k_B T / 6\pi\eta\alpha)$ was used, where k_B is the Boltzmann's constant, T is the temperature, α is the radius of the PFK-1.1 particle (which we roughly estimated as 5 nm based on Webb et al. (30)), and η is the viscosity. In comparing the calculated viscosity values, *p*-value was calculated using the Mann-Whitney *U* test.

Aspect ratio calculations and size measurement of PFK-1.1

The aspect ratio was calculated with the max projected images. After thresholding the images to obtain an outline for each punctum, the "Analyze Particles" function in ImageJ was used to calculate aspect ratio values for each punctum and for all time points. Considering the resolution limit of a spinning-disk confocal (~300 nm), any structure with a diameter less than 500 nm and an area smaller than 0.2 μm^2 was excluded from the analyses. PFK-1.1 condensate size or area was measured after thresholding the images and using the "Analyze Particles" function.

PFK-1.1 rate of formation, dispersion, and initiation time calculations

Using the acquired time-lapse videos of PFK-1.1 cluster formation and dispersion with the hybrid microfluidic-hydrogel device, change in the max fluorescence of individual clusters were tracked over time using ImageJ. From plotting the max fluorescence change over time and performing linear regression, the region of where max fluorescence increases (for the formation) or decreases (for the dispersion) linearly was identified using the following parameters: minimum slope of at least 5 (fluorescence intensity/s) and minimum length of half the time of the total treatment time. Any punctum with a starting fluorescence or pixel value of 1.2×10^5 AU was excluded from the calculations because the max fluorescence did not further peak after this value or quickly reached a saturation point. MATLAB (The MathWorks, Natick, MA) was used to conduct linear regression with the criteria as mentioned above. Rate was defined as the slope of the fitted line, and the initiation time was defined as the time for the first data point of the fitted line. The *p*-value comparing the rates of PFK-11. cluster formation and dispersion was calculated using the Mann-Whitney *U*-test.

RESULTS

PFK-1.1 localizes to specific subcellular compartments in vivo

To better understand the subcellular localization of glycolytic proteins in living animals, we generated transgenic *C. elegans* strains expressing functional fluorophore-tagged PFK-1.1 (PFK-1.1::EGFP) under its own promoter (Fig. S1 *A*). Expression of PFK-1.1::EGFP rescues synaptic vesicle cycle defects observed in *pfk-1.1* loss-of-function alleles, indicating that tagged PFK-1.1 is both functional and able to recapitulate the endogenous expression pattern of the gene ((19) and data not shown). In vivo examination of the PFK-1.1 expression pattern revealed, as expected, broad expression of PFK-1.1 in multiple tissue types, including muscles and neurons (Figs. 1 *A* and S1, *B* and *C*). In most examined tissues, there were high levels of cytoplasmic PFK-1.1 and no pronounced subcellular organization.

In some tissues, PFK-1.1 displayed subcellular organization. In muscles, PFK-1.1 localized into a striking pattern of longitudinal bands with alternating interdigitated foci (Fig. 1, *B* and *B′*), consistent with the protein being specifically enriched at two subcellular compartments: 1) M-lines within the A band of muscle sarcomeres and 2) dense body structures (functionally analogous to vertebrate Z-disks) (Fig. 1 *C*). M-lines and dense bodies function as anchors for thick myosin fibers and thin actin fibers, respectively, and their organization within muscle cells is necessary for filament cross-bridge formation and muscle contractions (31–34). Consistent with our observations, immunohistological studies in *Drosophila* have also shown that glycolytic proteins are enriched at M-lines and Z-disks in flight muscles (13).

To better examine the in vivo subcellular localization of endogenous PFK-1.1 in single cells, we generated conditional transgenic lines via CRISPR-Cas strategies (35–37). In brief, we used CRISPR-Cas to introduce two flippase recombinase target (FRT) sites that flank a transcriptional stop motif followed by a GFP sequence to the C-terminus of the endogenous *pfk-1.1* locus (Fig. S1 *D*). Introduction of these FRT sites did not result in detectable mutant phenotypes,

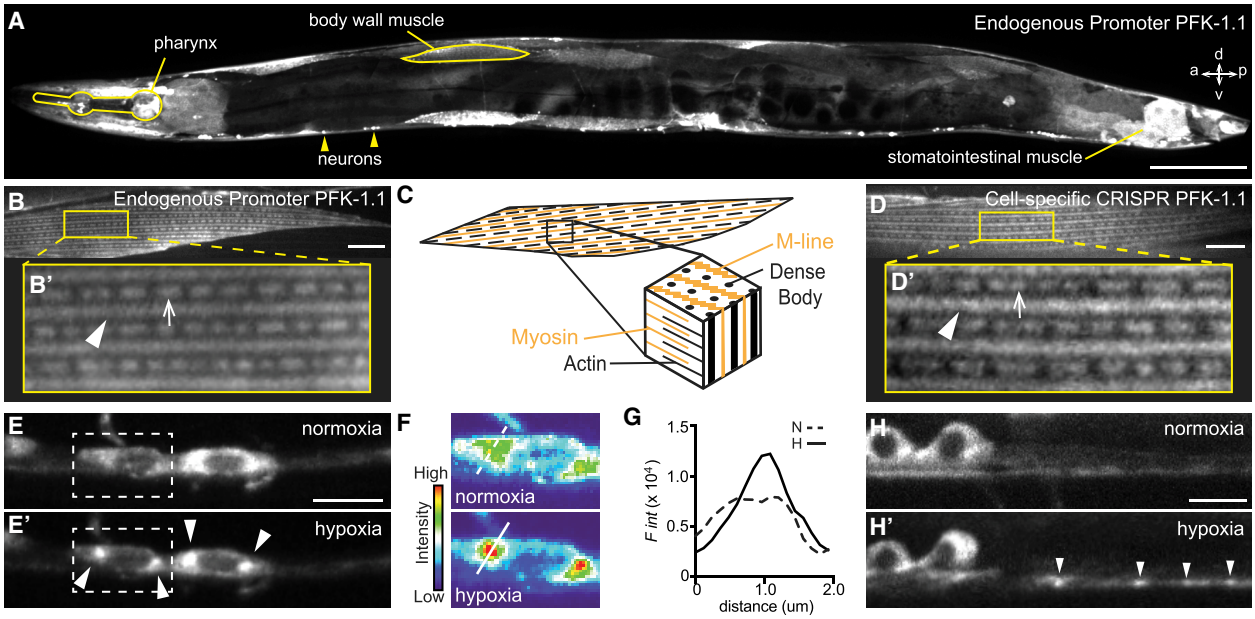

FIGURE 1 Subcellular localization of PFK-1.1 in neurons and muscles of *C. elegans*. (*A*) Localization of PFK-1.1::EGFP expressed under its own promoter in *C. elegans*, with specific tissues labeled. For orientation: anterior (a), posterior (p), dorsal (d), and ventral (v). Scale bars, 100 μm. (*B* and *B′*) *C. elegans* body wall muscle showing the localization of PFK-1.1 in M-lines (*arrowhead*) and dense bodies (*arrow*). PFK-1.1 was expressed under its own promoter. Scale bars, 10 μm. (*C*) A schematic showing the myofibrils of the *C. elegans* body wall muscle. M-line and dense bodies act as anchors for myosin and actin filament, respectively. (*D–H′*) The *mig-13* promoter was used in conditional CRISPR lines to tag the endogenous PFK-1.1 with GFP in a subset of tissues. (*D* and *D′*) Endogenous PFK-1.1 also localizes to M-lines (*arrowhead*) and dense bodies (*arrow*) in the body wall muscle. Scale bars, 10 μm. (*E* and *E′*) PFK-1.1 clusters form in the neuronal cell bodies (*arrowheads*) over time under hypoxia. Here, elapsed time of hypoxia was 55 min. (*F*) Pseudocolor based on fluorescence intensity of the dashed box in (*E*) for the two conditions. (*G*) Quantification of fluorescence intensity along the lines shown in (*F*) for each condition: N (normoxia) and H (hypoxia). (*H* and *H′*) PFK-1.1 clusters can be seen in the neurites (*arrowheads*) after hypoxia. Here, elapsed time of hypoxia was 10 min.

including the synaptic vesicle phenotype observed for the PFK-1.1 loss-of-function alleles (data not shown), suggesting that the genomic modifications do not alter PFK-1.1 expression or function. Using cell-specific promoters, we then drove the expression of flippase to excise the FRT-flanking transcriptional stop motif, allowing for the expression of the endogenous GFP-tagged PFK-1.1 in single cells (see Supporting materials and methods). Flippase expression using *mig-13* and *unc-47* promoters resulted in the expression of PFK-1.1::GFP in subsets of tissues and with a low signal because of endogenous labeling. Consistent with the localization pattern of the overexpressed PFK-1.1::EGFP (Fig. 1 *B*), we also observed the localization of PFK-1.1 at M-lines and dense bodies in the muscles of the cell-specific CRISPR lines (Fig. 1, *D* and *D′*).

We then examined the subcellular localization of PFK-1.1 in neurons. Expression of PFK-1.1:EGFP in single neurons revealed that although PFK-1.1 is not equally distributed throughout the neurite, it is, for the most part, diffusely localized in the cytosol (Fig. S1 *E*). Previously, we observed that under conditions known to cause energy stress, such as transient hypoxia, PFK-1.1 dynamically relocalizes to subcellular compartments (19). These former studies were done by overexpressing PFK-1.1 from cell-specific promoters in single neurons. Consistent with these observations, an examination of the conditional CRISPR lines revealed that upon transient hypoxia, endogenous PFK-1.1 relocalizes from a diffuse cytosolic pattern to subcellular clusters both in the neuronal soma and in neurites (Figs. 1, *E–H′* and S1 *F*).

Our findings demonstrate that in vivo and in metazoans, PFK-1.1 localizes to specific subcellular compartments. They also reveal that the localization pattern of PFK-1.1 varies between tissues. Importantly, our studies demonstrate that even in cells that have no obvious subcellular organization of PFK-1.1, such as the neurons, the localization of endogenous PFK-1.1 can dynamically change in response to cues within the cellular environment.

PFK-1.1 dynamically relocalizes to distinct subcellular compartments in response to transient hypoxia

Transient hypoxia inhibits oxidative phosphorylation at the mitochondria and induces cellular energy stress. To characterize the dynamic responses of PFK-1.1 to controlled changes in oxygen concentration, we developed a hybrid microfluidic-hydrogel device that enables precise regulation of oxygen concentration in the animal's surrounding environment during high-resolution and long-term imaging of

PFK-1.1 localization (Fig. 2, *A–C*; (26)). Calibration of our device enabled us to make precise and rapid switches between steady-state hypoxic (0% O_2) and normoxic (21% O_2) conditions within 1 min (Fig. S2, *A–D*). Animals under sustained steady-state normoxic conditions (21% O_2) did not show relocalization of PFK-1.1 proteins in neurons (Fig. S3 *A*), indicating that variables such as air flow or mechanical forces during mounting to the device do not affect the localization of PFK-1.1. Induction of transient hypoxia, however, resulted in robust relocalization of PFK-1.1 in neurons from a diffuse state in the cytoplasm into distinct clusters near synapses (Fig. 2 *D*). The increased signal of PFK-1.1 near synapses was not the result of an increase in total protein levels at the neurite because the total fluorescence in the neurite did not increase upon hypoxic stimuli (Fig. S2 *E*).

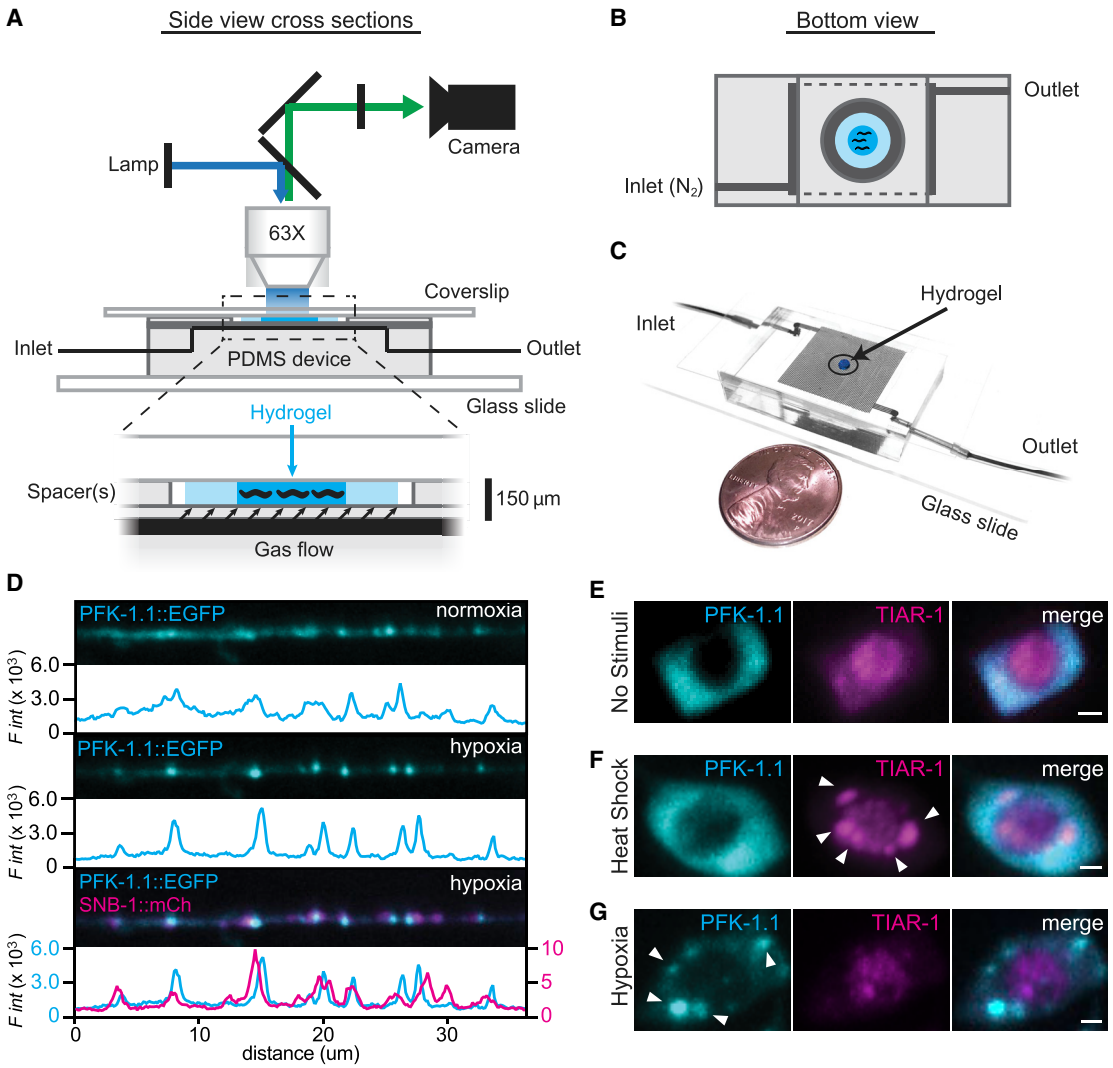

FIGURE 2 Hybrid microfluidic-hydrogel device enables high-resolution imaging of PFK-1.1 localization and clustering dynamics during transient hypoxia. (*A*) A schematic of the hybrid microfluidic-hydrogel device used to induce transient hypoxic conditions in *C. elegans* while imaging PFK-1.1 continuously and at high resolution. Zoom-in (*below*) shows micron-scale device geometries for animal immobilization, gas delivery, and imaging. (*B*) A bottom view schematic of the device shows geometry of inlet and outlet channels connected to the gas arena (*dark gray area*). Animals are immobilized in hydrogel (*dark blue*) surrounded by buffer (*light blue*) and sealed by a circular, hole-punched PDMS spacer. Oxygen conditions experienced by the animals are controlled by inlet gas flow. (*C*) A picture of the microfluidic device, size comparable to a penny, with inlet and outlet tubing connected. (*D*) PFK-1.1::EGFP (*cyan*) in GABAergic neuron under normoxia (*top panels*) and after 10 min of transient hypoxia (*middle panels*). Coexpression with synaptobrevin-1/SNB-1::mCh (*magenta*, *lower panel*) shows that PFK-1.1 relocalized into clusters near synaptic sites upon transient hypoxia. Corresponding fluorescence intensity for each image is shown immediately below the corresponding image, with colors matching traced protein distribution in the image. (*E*) PFK-1.1::mRuby-3 (*cyan*) and TIAR-1::EGFP (*magenta*) in the cell body of neurons with no stimuli (normoxic conditions and 22°C). (*F*) Heat shock (37°C for 1 h) leads to formation of stress granules, as observed with TIAR-1 aggregates (*arrowheads*). PFK-1.1 does not form clusters under this condition. (*G*) Under transient hypoxic conditions (25–45 min), PFK-1.1 forms clusters in the cell body (*arrowheads*) that do not colocalize with TIAR-1. All scale bars, 1 μm.

Cellular stress is known to cause the aggregation of cytoplasmic RNAs and proteins into stress granules (38). To examine whether PFK-1.1 in neurons was relocalizing into stress granules, we simultaneously imaged PFK-1.1 and the stress granule protein, TIAR-1, under heat shock conditions known to cause stress granule formation (39,40). Consistent with previous studies, TIAR-1 in neurons was enriched in the soma and could be seen in both the cytoplasm and nuclei (Fig. 2 *E*). Heat shock by incubating worms at 37°C for 1 h resulted in the aggregation of TIAR-1 in both the cytoplasm and nuclei, as expected. However, PFK-1.1 did not form clusters under conditions that caused TIAR-1 aggregation (Fig. 2 *F*). We then examined whether stress granules are formed upon transient hypoxic conditions known to induce PFK-1.1 clustering. TIAR-1 has been shown to aggregate under several hours of prolonged hypoxic conditions, but not under transient hypoxia (41,42). Consistent with those reports, we observed that although transient hypoxia (less than 20 min) caused PFK-1.1 clustering, the same hypoxic conditions did not cause TIAR-1 clustering (Fig. 2 *G*). Lack of colocalization was also observed between PFK-1.1 and stress granule markers TDP-43 and G3BP1 (data not shown). Our findings demonstrate that TIAR-1 and PFK-1.1 cluster under different cellular conditions and suggest that PFK-1.1 clusters correspond to a new subcellular compartment distinct from stress granules.

PFK-1.1 reversibly organizes into biomolecular condensates

To examine the dynamics of PFK-1.1 clusters, we performed high-resolution time-lapse imaging of PFK-1.1 in single neurons of living animals upon transient hypoxia exposure. We focused our analyses in 3 μm neurite regions that displayed PFK-1.1 enrichment during normoxia. We observed that induction of transient hypoxia resulted in a redistribution of the PFK-1.1 protein within these regions, with PFK-1.1 concentrating into 0.5–1 μm compartments (Fig. 3, *A* and *B*). We also observed a concomitant decrease of PFK-1.1 levels in regions adjacent to the emerging compartments (Fig. 3 *C*). A kymograph of PFK-1.1 in neurites showed that the local formation of PFK-1.1 clusters, which remained relatively immobile, was due to a redistribution of diffuse PFK-1.1 proteins to concentrated compartments (Fig. 3 *D*). Together, our results indicate that PFK-1.1 puncta emerge through the local condensation of PFK-1.1 material into concentrated clusters, which we now refer as condensates (2,43).

We observed that condensates of PFK-1.1 were visible within 5 min of transient hypoxia. The persistence of hypoxic treatment resulted in the emergence of additional condensates, resulting in the almost complete relocalization of all visible PFK-1.1::EGFP into clusters (Fig. 3 *E*). Interestingly, restoring animals to normoxic conditions resulted in the dispersion of PFK-1.1 in the cytosol in both the neurite and cell body (Figs. 3 *E* and S3 *B*; Video S1). Thus, we asked whether PFK-1.1 proteins were capable of repeated cycles of condensation and dispersion in neurons. We observed that PFK-1.1 could undergo multiple cycles of condensation, displaying similar dynamics in each cycle (Fig. 3 *F*; Video S2). Importantly, during the two rounds of transient hypoxia and normoxia, we observed that PFK-1.1 condensates reappeared in similar locations (Figs. 3 *G* and S3 *C*). The repeated formation of PFK-1.1 clusters at the same location in the neurite occurred even after PFK-1.1 proteins completely diffused back to their initial state (Fig. S3 *D*). The reappearance of PFK-1.1 clusters at the same sites is consistent with our observations that PFK-1.1 clusters form preferentially (but not exclusively) near synapses (Fig. 2 *D*; (19)). The observation may suggest the existence of synaptic nucleating factors or the existence of subcellular conditions at the synapse that instructs local assembly of PFK-1.1 upon transient hypoxia.

PFK-1.1 condensates exhibit liquid-like behaviors

Biomolecular condensates, including the nucleolus, germ granules, prion proteins, and postsynaptic proteins, have been shown to exhibit liquid-like characteristics (29,44–47). To examine whether PFK-1.1 condensates transiently induced by hypoxic treatment also exhibit liquid-like properties, we tested for the three key features that define liquid-like compartments: 1) liquid-like compartments are spherical because of surface tension and deformed because of cellular geometry constraints, 2) they can fuse and relax into a single spherical droplet, and 3) they exhibit fast internal molecular rearrangements (48). We systematically tested the PFK-1.1 clusters for their biophysical characteristics.

Liquid-like compartments are spherical because of surface tension and deformed because of cellular geometry constraints

Our qualitative observations on the emerging clusters revealed that most of the PFK-1.1 condensates were circular (and, because there was no obvious z axis asymmetry, likely spherical). To examine the shape of the PFK-1.1 condensates and to establish a quantitative criterion that defines the emergence of the clusters during condensation of PFK-1.1, we computed the aspect ratio, a ratio between the major and minor axes of the emerging clusters, over time (Figs. 4 *A* and S4, *A* and *B*; (44,49)). Only the condensates with sizes above the diffraction limit were quantified (see Materials and methods). Aspect ratio calculations of hypoxia-induced PFK-1.1 clusters in neurites revealed a distribution with a mean aspect ratio of 1.32 $\pm$ 0.04 (mean $\pm$ SEM; N = 38) (Fig. 4 *B*). A perfect sphere has an aspect ratio of 1, so our data suggest that PFK-1.1 clusters were similar, on average, to elongated spheroids.

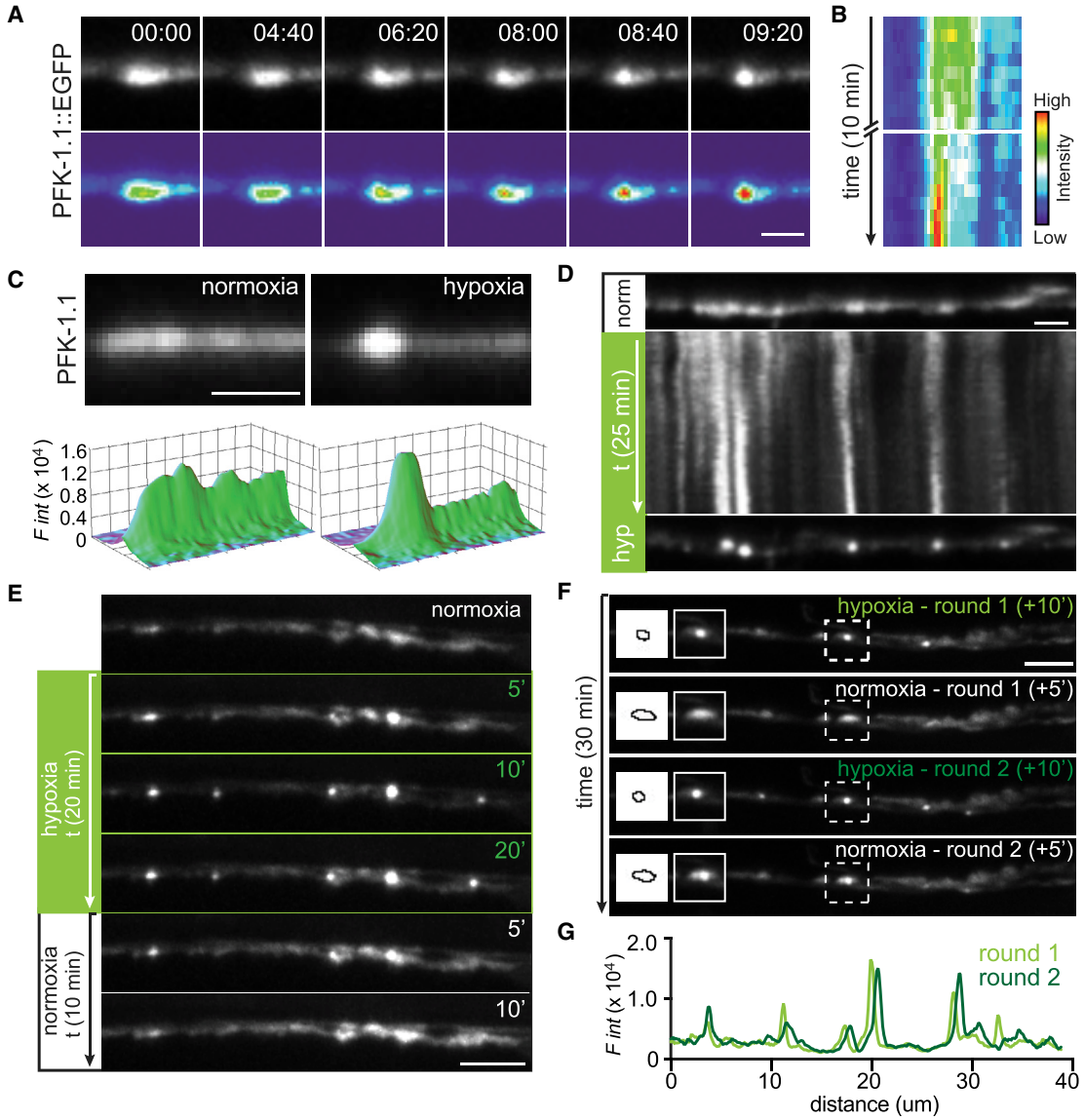

FIGURE 3 PFK-1.1 reversibly organizes into biomolecular condensates. (*A*) Upon minutes of transient hypoxia, PFK-1.1 relocalizes from a dispersed localization pattern in the cytosol to a concentrated punctum. Time elapsed is indicated for each image in minutes:seconds. Bottom images have been pseudocolored based on fluorescence intensity. Scale bars, 2 μm. (*B*) A kymograph of PFK-1.1 localization shown in (*A*) over 10 min of transient hypoxia. 0–3 and 7–10 min are shown. (*C*) Localization of PFK-1.1 in a neurite during normoxia (*left panel*) and after 18 min of transient hypoxia (*right panel*). Corresponding three-dimensional surface rendering projections of fluorescence intensity in panels below. Scale bars, 1 μm. (*D*) Kymograph showing PFK-1.1 localization change over time, starting from normoxic condition (norm, *top panel*) to 25 min of transient hypoxia (hyp) (*kymograph* and *lower panel*). Scale bars, 2 μm. (*E*) Localization of PFK-1.1 through a normoxia-hypoxia-normoxia cycle at different time points (as indicated by minutes in *upper right hand* of images). PFK-1.1 condensates induced by transient hypoxic condition (*green numbers*, in minutes) can be seen dispersing away when the condition is returned to normoxia (white numbers, in minutes). See also Video S1. Scale bars, 5 μm. (*F*) PFK-1.1 localization under two cycles of transient hypoxia (rounds 1 and 2). PFK-1.1 forms condensates during 10 min of transient hypoxia and becomes diffuse during 5 min of normoxia. Dashed box in main panel corresponds to zoomed in image on the left (along with the outline of the corresponding morphology of the condensate). See also Video S2. Scale bars, 5 μm. (*G*) Line scan of first round (*light green*) and second round (*dark green*) of PFK-1.1 condensate localization in the neurite shown in (*F*) under transient hypoxic conditions. Note that during repeated cycles of normoxia and transient hypoxia, PFK-1.1 condensates reappear at similar subcellular locations.

Because we qualitatively also observed a relationship between the size of the puncta and the extent of the elongated spheroids (Fig. S4 *C*), we hypothesized that neurite space constraints could affect the shape of the larger (liquid) PFK-1.1 condensates. Liquids are capable of deformation, and liquid droplets confined within a cylindrical-like space such as a neurite would be expected to elongate into capsule-shaped spherocylinders. To test whether the larger PFK-1.1 condensates were constrained capsule-shaped spherocylinders, we first calculated the average diameter

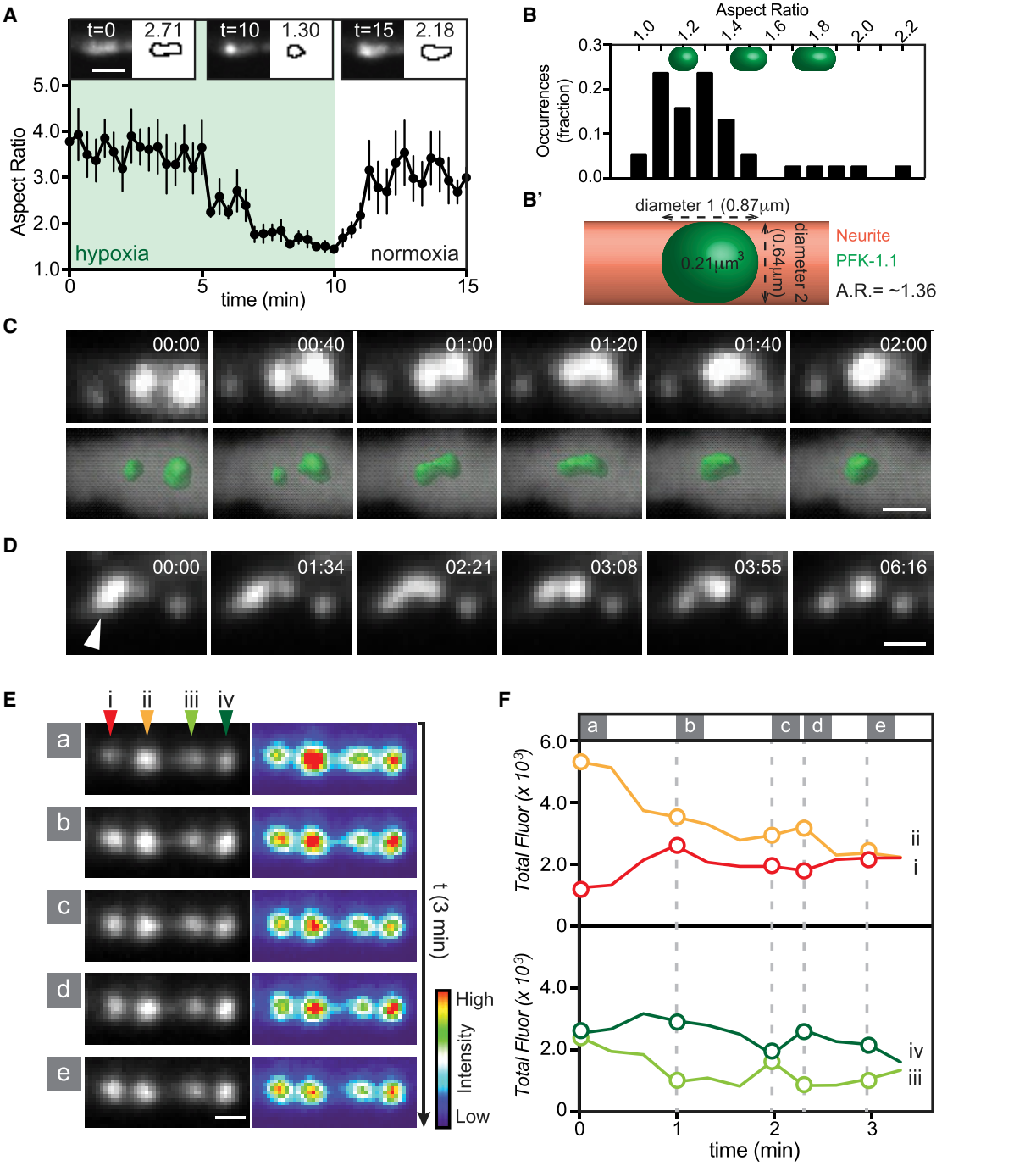

FIGURE 4 PFK-1.1 condensates exhibit liquid-like behaviors. (*A*) Reversibility of PFK-1.1 localization as quantified by the aspect ratio of a population of PFK-1.1 condensates through one cycle of hypoxia-normoxia (N = 8 condensates). Mean (*black circles*) and SEM values are shown for each time point. Images on top and corresponding outlines are representative morphologies of condensates: from left to right, the beginning of hypoxia, after 10 min of transient hypoxia, and after 5 min of recovery in normoxia. Scale bars, 2 μm. (*B*) A histogram of the fraction of occurrence of the PFK-1.1 condensate aspect ratio after 40 min of transient hypoxia (N = 38 condensates). A perfect sphere has an aspect ratio of 1, and PFK-1.1 condensates have an average aspect ratio of 1.3. Representative spherocylindrical shapes for different aspect ratios (1.2, 1.5, and 1.8) are shown above. (*B′*) Schematic and calculation of aspect ratio for a theoretical spherical PFK-1.1 condensate with a volume of 0.21 μm^3 that fits into a neurite with a diameter of 0.64 μm. Corresponding predicted aspect ratio (A.R.) is 1.36. (*C*) Time-lapse images of adjacent PFK-1.1 condensates under transient hypoxic conditions fusing and relaxing into a spheroid (*above*) and their corresponding three-dimensional surfaced rendered images (*below*). Elapsed time from the beginning of the imaging session is shown for each image in minutes:seconds. Here, 00:00 is 08:40 into the hypoxic treatment. See also Video S3. Scale bars, 1 μm. (*D*) A fluid-like movement recorded for a PFK-1.1 condensate (*arrowhead*) during transient hypoxia. Elapsed time from the beginning of the imaging session is indicated for each image in minutes:seconds.

(legend continued on next page)

of the neurites by measuring cytoplasmic mCherry expressed in GABAergic neurons, and by examining electron micrographs of GABAergic neurites (50). From these calculations, we determined the average diameter of the examined neurites to be 0.64 ± 0.06 μm (mean ± SEM; N = 20) (Fig. S4 *D*). Empirical measurement of the area of the PFK-1.1 condensates (see Supporting materials and methods) revealed that these structures had an average area of 0.43 ± 0.04 μm^2 (mean ± SEM; N = 38) (Fig. S4 *E*). Assuming radial symmetry of the neurite, the average condensate volume would be 0.21 ± 0.03 μm^3, which is larger than the maximum sphere fitting within the neurite diameter, 0.14 ± 0.04 μm^3. A hypothetical spherocylinder with a volume of 0.21 μm^3 and radial diameter of 0.64 μm would have a length of 0.87 μm and an aspect ratio of 1.36 (Fig. 4 *B′*), a value similar to the one we empirically calculated, which was 1.32. Of note, the spherocylinder represents an optimal geometry for the condensate in the context of the constraints of the neurite because this shape minimizes surface area as compared to several smaller spherical droplets of equal volume. Thus, our findings suggest that PFK-1.1 condensates have liquid-like properties that result in spherocylindrical morphologies because of constraints by two physical forces: the surface tension of the condensate and the dimensions of the neurite.

Liquid-like structures can fuse and relax into a single spherical droplet

Phase-separated compartments display stereotypical fluid-like behaviors that include fusion. We reasoned that if PFK-1.1 condensates displayed liquid-like characteristics, condensates that happened to nucleate in close proximity (within one micron from each other) would fuse. Indeed, PFK-1.1 condensates that came into physical contact fused into new, larger clusters (Figs. 4 *C* and S5, *A* and *B*; Videos S3 and S4). Quantification of the total area of the two PFK-1.1 condensates before fusion was similar to the total area of the single PFK-1.1 condensate postfusion (Fig. S5 *C*). The new clusters relaxed into spheroid shapes (within the geometrical constraints of the neurite) upon fusion, consistent with a thermodynamically favored response of a liquid compartment to surface tension (29). Moreover, whereas most PFK-1.1 particles in vivo retained spheroid shapes upon formation, some particles would occasionally become deformed and even shear, presumably because of cytoplasmic flux or transport of organelles disrupting the PFK-1.1 condensates in the tightly packed spaces of the neurite (Figs. 4 *D* and S5 *D*). Shearing of droplets might represent an interaction between the phase-separated condensates and the cellular medium, which could occasionally provide an energetic cost that favors the formation of smaller droplets (51–53). Importantly, deformation of the condensates resulted in transient fluid-like movements and eventual relaxation back into spheroid structures.

Quantification of the levels of fluorescence in nearby condensates revealed that growth of a condensate happened at the expense of adjacent condensates in a process that was reminiscent of Ostwald ripening (Fig. 4 *E*). But unlike Ostwald ripening, which is a thermodynamically spontaneous process in which smaller droplets dissolve into energetically favored larger droplets (54), some PFK-1.1 condensates in vivo did not result in larger droplets. Instead, the exchange of material reached a dynamic equilibrium between adjacent condensates as they approached similar fluorescence levels (Fig. 4, *E* and *F* and Video S5). The observed in vivo dynamics between adjacent condensates could be because of active cellular processes that drive the formation of two similar condensates (55,56), or because of other unidentified phenomena. Importantly, the exchange of material between adjacent clusters is consistent with liquid-like behaviors of the PFK-1.1 condensates.

Liquid compartments exhibit fast internal molecular rearrangements

To further probe the molecular dynamics of PFK-1.1 condensates, we performed FRAP experiments. We observed that upon partial FRAP of the PFK-1.1 condensate, fluorescence in the bleached area recovered within seconds of postbleaching (Figs. 5, *A* and *B* and S5, *E* and *E′*). Consistent with an internal rearrangement resulting in fluorescence recovery, we observed that fluorescence in the bleached region increased at the expense of the unbleached areas (Fig. 5 *C*). The observed molecular dynamics for PFK-1.1 within condensates suggest that PFK-1.1 remains in liquid phase droplets capable of undergoing internal dynamic rearrangements (29).

PFK-1.1 condensates harden with time

To test whether transient hypoxia was inducing a change in the molecular dynamics of PFK-1.1 resulting in liquid-liquid phase separation, we measured the half-time recovery and lateral diffusion of PFK-1.1 in its soluble state during normoxia versus its condensate state during hypoxia by partially photobleaching the condensates (29). Using FRAP, we determined that the average half-time recovery in the photobleached regions for diffusely localized PFK-1.1 was 0.6 s, whereas in the condensate, it was 3.8 s (data not shown). Our findings indicate a substantial change

Scale bars, 1 μm. To see all frames recorded, refer to Fig. S5 *D*. (*E*) Four adjacent PFK-1.1 condensates (*i–iv*) during transient hypoxia displayed exchange of PFK-1.1::EGFP in the span of 3 min. The first image (*a*) is after approximately 6 min into hypoxic treatment. See also Video S4. Scale bars, 1 μm. (*F*) Quantification of the fluorescence of the PFK-1.1 condensates in (*E*), with graphs pseudocolored to corresponding arrowheads in (*i*)–(*iv*) and time points (*a*)–(*e*) in (*E*).

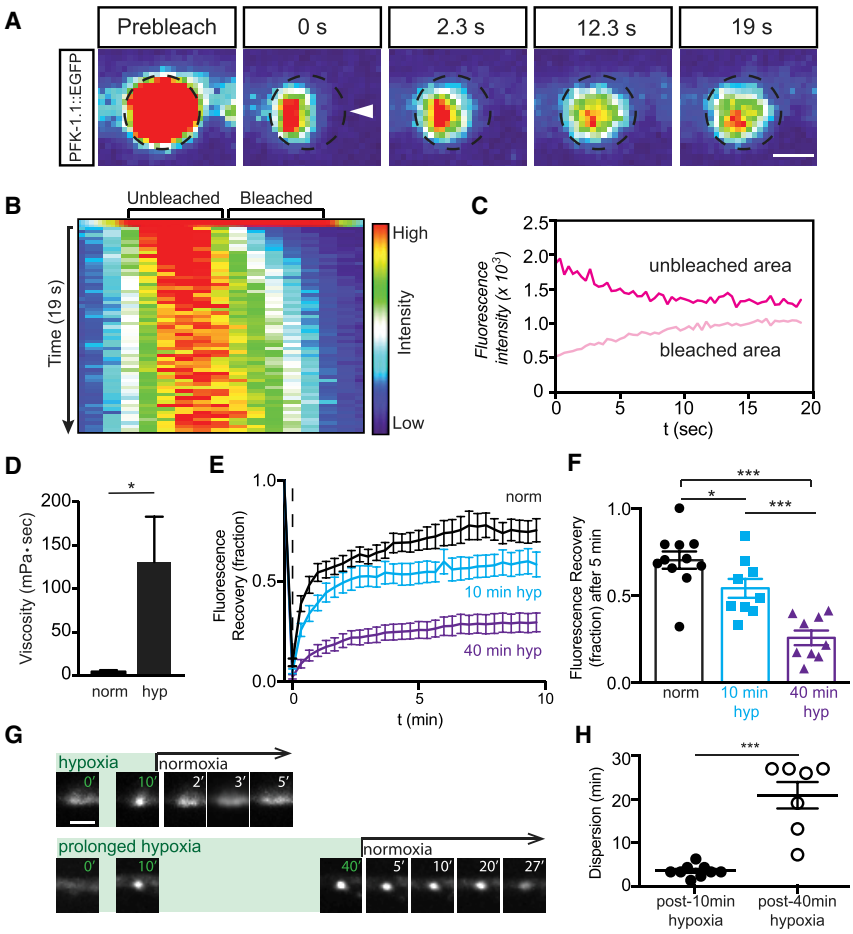

FIGURE 5 PFK-1.1 compartments exhibit fast internal molecular rearrangements that harden with time. (*A*) FRAP of a PFK-1.1::EGFP condensate after 10–20 min of transient hypoxia. PFK-1.1::EGFP condensate initial shape is outlined with dashed circle, and partial area bleached is highlighted with arrowhead in second panel. Scale bars, 1 μm. (*B*) A kymograph of fluorescence distribution across the bleached punctum in (*A*). (*C*) Change in fluorescence values for the unbleached region (*dark pink line*) and the bleached region (*light pink line*) of the condensate in (*A*) over time (seconds). (*D*) Viscosity estimates of PFK-1.1 proteins under normoxia (labeled "norm") and 10–20 min of transient hypoxia (labeled "hyp"). (N = 4 neurons for each conditions). (*E* and *F*) FRAP of cytosolic PFK-1.1 after normoxia (*black line*, labeled "norm"), PFK-1.1 condensate after 10 min of transient hypoxia (*blue line*, labeled "10 min hyp"), and PFK-1.1 condensate after 40 min of transient hypoxia (*purple line*, labeled "40 min hyp") and corresponding fraction of fluorescence recovery 5 min postbleaching calculated in (*F*). In all experiments, PFK-1.1 was photobleached to a minimum of 80% of its original fluorescence value. Note how recovery dynamics decrease with increased exposure to transient hypoxia, suggesting that PFK-1.1 condensates harden with time. (*G*) Comparison of PFK-1.1 condensate reversal in normoxia after 10 min (*top row*) and 40 min (*bottom row*) of hypoxia (marked by *green*). Time (in minutes) for each image is indicated on the top right corner, and corresponding images displaying dispersion due to normoxia are shown for the two conditions examined (10 min of hypoxia in the *top row*, and 40 min of hypoxia in the *bottom row*). Scale bars, 2 μm. (*H*) Quantification of the time it takes for PFK-1.1 condensates to disperse upon return to normoxia when condensates were formed under 10 min of hypoxia (*black circles*; N = 9) or 40 min of hypoxia (*open circles*; N = 7). Error bars denote SEM. $*p < 0.05$. $**p < 0.01$. $***p < 0.001$ between indicated groups.

in the diffusion dynamic of PFK-1.1 between normoxia and hypoxia and are consistent with changes in molecular dynamics during condensation.

To approximate the fluidity of PFK-1.1 under the two states, we used the Stokes-Einstein equation (see Materials and methods) to estimate the viscosity of PFK-1.1. Although the accuracy of the viscosity calculations is limited by the small size of the puncta, we note that, in the soluble state, PFK-1.1 had an estimated viscosity of 4.8 ± 1.7 mPa • s (mean ± SEM; N = 4), which is ~5 times more viscous than water. This value is comparable to the reported viscosity (2.0–3.0 mPa • s) of the cytoplasm (57), consistent with PFK-1.1 being largely diffusely localized in the cytosol under normoxic conditions. Upon transient hypoxic conditions, however, the calculated viscosity for PFK-1.1 was 130.5 ± 52.1 mPa • s (mean ± SEM; N = 4) (Fig. 5 *D*). Our findings suggest that PFK-1.1 increases two orders of magnitude in viscosity after it forms condensates. Importantly, our findings indicate that the biophysical properties of PFK-1.1 change upon transient hypoxia and suggest that these changes could contribute to PFK-1.1 relocalizing into phase-separated condensates.

Changes in the viscoelastic properties of molecular condensates contribute to liquid-liquid phase separation. Yet, it has also been documented that changes in the material phase of the condensates can contribute to their maturation into more "gel-like" or "solid-like" states that eventually result in the (pathological) aggregation of proteins (45,58). We reasoned that if transient hypoxia was inducing a change in the molecular dynamics of PFK-1.1, one would expect that conditions of prolonged hypoxia would further alter the molecular dynamics and the biophysical properties of the condensates. To test whether prolonged hypoxia alters the PFK-1.1 dynamics, we compared the fluorescence recovery of PFK-1.1 condensates that were fully photobleached after 10 min (newly formed condensates) and 40 min ("mature" condensates) of hypoxic treatment. We observed that the recovery dynamics of mature PFK-1.1 condensates were significantly slower than those of newly formed condensates (Figs. 5, *E* and *F* and S6 *A*). The slower recovery dynamics due to prolonged hypoxia are consistent with an increase in the immobile fraction, which could be from changes in the state of the liquid condensates into solid or gel-like states. Also supportive of a change in PFK-1.1

condensate into solid or gel-like state, we observed that PFK-1.1 condensates formed during 10 min of hypoxia required an average of 3.2 ± 0.5 min (± SEM; N = 9) in normoxia before dispersion was observed, whereas PFK-1.1 condensates formed and maintained during 40 min of hypoxia required an average of 20.9 ± 3.1 min (± SEM; N = 7)) for dispersion (Fig. 5, *G* and *H*). Our findings are consistent with the increased viscosity observed for newly formed PFK-1.1 condensates (Fig. 5 *D*) and suggest that changes in the viscoelastic properties of PFK-1.1 contribute to the biophysical properties of the condensates, including transitions into liquid-like or gel-like states.

In the course of our studies, we also imaged mature condensates that happened to be adjacent to one another. These condensates sometimes came into physical contact with each other, just as we had previously documented for the fusion events occurring in newly formed condensates (Fig. 4 *C*). Interestingly, however, and unlike the newly formed condensates, some of these mature condensates deformed and "bounced" off each other upon contact (Fig. S6 *B*; Video S6). Our observations of these dynamics suggest that the viscoelastic properties of PFK-1.1 condensates change upon persistent hypoxia.

Local concentration of PFK-1.1 correlates with the initiation time of condensates

Physical principles of phase transitions influence the assembly of membraneless organelles such as p-granules and the nucleolus (59). A key biophysical aspect that influence the dynamics of membraneless organelle assembly is protein concentration (43,48,60). Because we observed a nonhomogeneous distribution of PFK-1.1 proteins throughout the neurite even during normoxia (Fig. S1 *E*), we hypothesized that PFK-1.1 concentration may influence cluster formation at subcellular regions. To test this hypothesis, we monitored the formation of PFK-1.1 condensates for specific subcellular regions that had varying concentrations of PFK-1.1 under conditions of persistent hypoxia (see Materials and methods). From the lengthened hypoxic treatment, we observed a continuous and asynchronous formation of PFK-1.1 condensates throughout the neurite, with PFK-1.1 condensates forming at different time points in different cellular regions (Fig. 6, *A* and *B*; Video S7). Comparisons of the local concentration of PFK-1.1 proteins in specific subcellular regions of the neurite, and the time at which the PFK-1.1 condensates initiate in those regions, revealed an inverse correlation between these two variables (Fig. 6 *C*). Our findings are consistent with initial PFK-1.1 concentrations affecting the time of initiation of the condensates, with a higher level of PFK-1.1 proteins corresponding to an earlier appearance of PFK-1.1 condensates.

Interestingly, we also observed that once PFK-1.1 condensates appeared and regardless of where or when they appeared in the neurite, they underwent similar linear rates of increase in protein fluorescence. The constant increase of fluorescence did not vary based on the starting concentration and instead displayed a normal distribution around an average constant rate (Fig. 6 *D*). Furthermore, calculations of the rates of PFK-1.1 dispersion upon return to normoxic conditions also showed a normal distribution around an average rate that was similar to the average rate of condensation (Fig. 6, *E* and *F*).

Together, we found two properties regarding the local emergence of PFK-1.1 condensates across subcellular regions: 1) concentration, which correlates with the timing of initiation of PFK-1.1 condensates, and 2) rates of PFK-1.1 condensate growth (during transient hypoxia) and dispersion (during normoxia), which share a similar normal distribution regardless of initial concentration at subcellular locations. Thus, the asynchronous formation of PFK-1.1 condensates throughout the neurite could result from the initial uneven distribution of PFK-1.1 in neurites, which in turn determines the local concentration and the initiation time of PFK-1.1 condensates.

PFK-1.1 and aldolase are interdependent for the formation of glycolytic condensate

Multivalent interactions between proteins or proteins and RNAs play important roles in driving condensates into liquid-like protein droplets (2). Multivalent interactions can be mediated via folded protein domains, or intrinsically disordered regions with multiple interacting motifs (48,61–67). These interactions leading to phase separation can be recapitulated in vivo and in vitro by engineering self-association domains (63,68,69), underscoring the importance of multivalent interactions in the formation of condensates. PFK-1.1 does not have predicted intrinsically disordered but is a protein with dihedral symmetry capable of forming higher-order oligomers via multivalent interactions (21,70–72).

To test whether multivalent interactions could induce the formation of PFK-1.1 condensates, we tagged PFK-1.1 with cryptochrome 2 (CRY2), a class of flavoproteins from *Arabidopsis thaliana* that are capable of mediating oligomerization (73). Optogenetic control of CRY2 has been used to drive phase separation of intrinsically disordered proteins (69). The extent of CRY2-induced oligomerization depends on the protein that the CRY2 is fused to, and it has been observed that tetrameric proteins highly enhance the homo-oligomerization of CRY2 (74,75). We observed that CRY2-tagged PFK-1.1 formed condensates even in the absence of any light stimulation and under normoxic conditions (Figs. 7, *A* and *F* and S7 *A*). We also note that the PFK-1.1 condensates promoted by CRY2 were functional and capable of rescuing the synaptic vesicle phenotype in *pfk-1.1(ola72)* mutant animals (Fig. 7 *B*). Interestingly, the CRY2-tagged PFK-1.1 condensates localized to the synapse (Fig. S7 *A*), suggesting the existence of signals or scaffolds

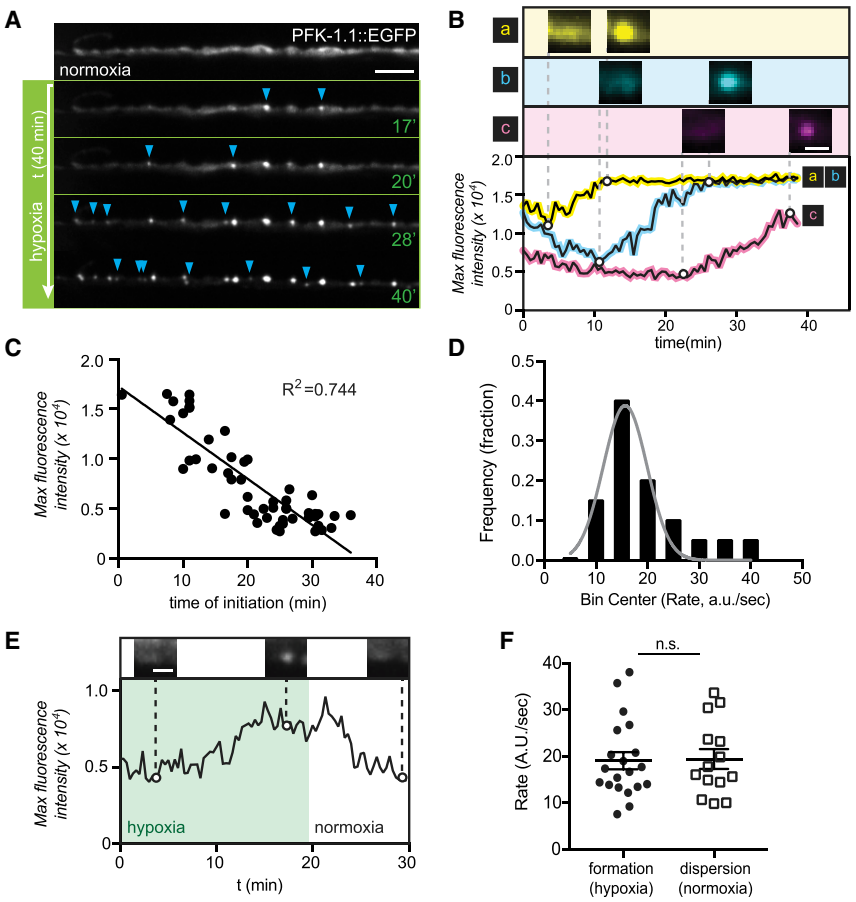

FIGURE 6 Local concentration of PFK-1.1 drives initiation of condensates. (*A*) PFK-1.1 dynamics through persistent hypoxia. Blue arrowheads mark newly formed PFK-1.1 condensates at each time point (*green numbers* indicate minutes into hypoxic treatment), indicating asynchronous formation of PFK-1.1 condensates throughout the neurite. Scale bars, 5 μm. See also Video S7. (*B*) Three separate regions in neurites, where PFK-1.1 condensates appear, are shown (*a–c*). The corresponding maximum fluorescence value over time for the three regions is shown below, pseudocolored to correspond to the region specified above (also labeled with *a–c*). PFK-1.1 condensate formation occurred with a linear increase in maximum fluorescence intensity through time in response to transient hypoxia. Scale bars, 1 μm. (*C*) The maximum fluorescence intensity of PFK-1.1::EGFP just before PFK-1.1 condensates are observed was plotted and compared with the time when PFK-1.1 condensates first appear (time of initiation). Note how the time of initiation negatively correlates with the maximum fluorescence intensity (equivalent to the amount of PFK-1.1 in a specific region of the neurite where PFK-1.1 condensates appear). (*D*) Rates for PFK-1.1 condensate formation were calculated for 20 condensates as maximum fluorescence intensity change over time, and their distribution was plotted. The rates are constant, regardless of initial concentration, and a normal (Gaussian) distribution (N = 20 condensates). (*E*) Maximum fluorescence intensity of a PFK-1.1 condensate calculated over time (minutes) during transient hypoxia (*shaded green*) and subsequent return to normoxic conditions. Representative images of PFK-1.1 condensates are shown for given time points above the graph. (*F*) Rates of formation and dispersion of PFK-1.1 condensates under transient hypoxia (*green circles*, *left*) and normoxia (*white squares*, *right*), respectively. Note how the rates of formation and dispersion are both constant, normally distributed (compare with *D*) and not significantly (specified as n.s. in graph) different. Error bars denote SEM.

that spatially instruct the site of phase separation, even when promoted by CRY2. These results indicate that PFK-1.1 self-association via CRY2 is sufficient to drive its condensation even in the absence of stimuli, and result in functional condensates capable of sustaining the synaptic vesicle cycle at synapses.

We then asked whether the PFK-1.1::mCherry::CRY2 ectopic condensates were sufficient to drive condensation of non-CRY2-tagged glycolytic proteins. We examined this by simultaneously expressing PFK-1.1::mCherry::CRY2 and PFK-1.1::EGFP in single neurons. As a control, we expressed mCherry::CRY2 along with the examined glycolytic protein. We observed that in neurons expressing mCherry::CRY2 and PFK-1.1::EGFP, PFK-.1.1 remained diffusely localized in the cytoplasm under normoxia, as expected (Fig. 7, *C* and *D*). However, in neurons coexpressing PFK-1.1::mCherry::CRY2 and PFK-1.1::EGFP, ectopic PFK-1.1::mCherry::CRY2 condensates recruited PFK-1.1::EGFP even under normoxia (Fig. 7, *A* and *D*).

Is recruitment of PFK-1.1 to condensates necessary for the recruitment of other glycolytic proteins? We used the microfluidic setup to simultaneously examine PFK-1.1 and glycolytic protein aldolase/ALDO-1. Aldolase, like PFK-1.,1, is diffusely localized in the cytosol under normoxic conditions. Upon transient hypoxia, we observed that the two glycolytic proteins condense at the same sites and with similar recruitment kinetics (Fig. 7 *E*; Video S8).

We then examined whether recruitment of PFK-1.1 to condensates depends on ALDO-1 by observing PFK-1.1 localization in *aldo-1* loss-of-function mutants. Interestingly, PFK-1.1 condensate formation was suppressed in *aldo-1(tm5782)* mutant animals, suggesting a requirement for ALDO-1 in PFK-1 recruitment (Figs. 7 *F* and S7, *B* and *C*). Similarly, ALDO-1 condensate formation was suppressed in *pfk-1.1(tm5741)* loss-of-function mutants, indicating a requirement for PFK-1.1 in the recruitment of ALDO-1 (Figs. 7 *G* and S7, *B* and *C*). Together, our findings indicate that PFK-1.1 and ALDO-1 genetically interact to recruit each other into condensates.

Is PFK-1.1 condensation sufficient to recruit other glycolytic proteins, like ALDO-1, into the condensates? We expressed PFK-1.1::mCherry::CRY2 and ALDO-1:GFP and observed that even under normoxic conditions, when PFK-1.1 condensates are facilitated by CRY-2, ALDO-1

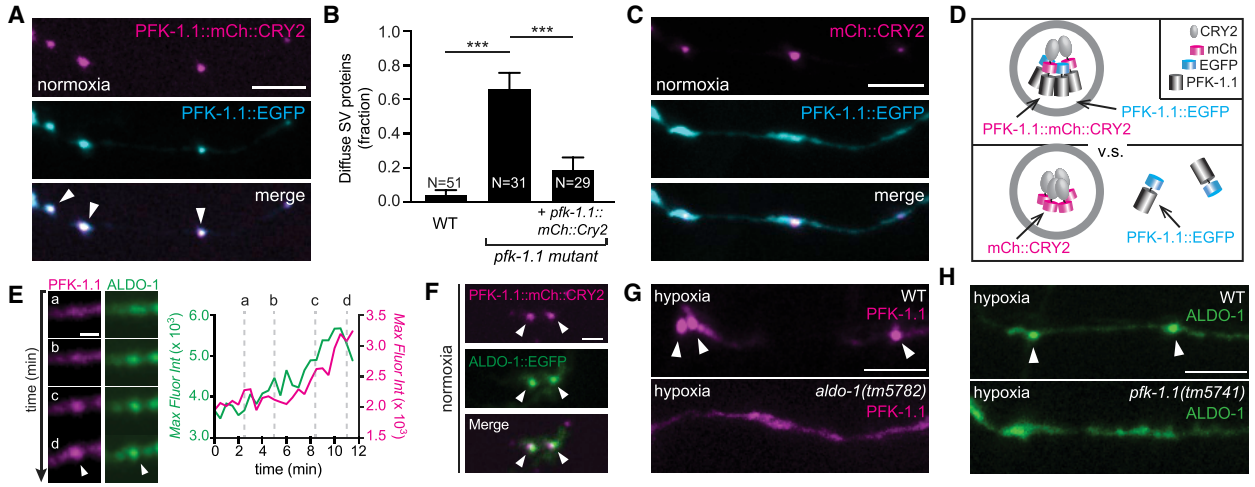

FIGURE 7 PFK-1.1 and aldolase condensate formation. (*A*) Under normoxia, PFK-1.1::mCh::CRY2 (*magenta*, *top panel*) is sufficient to cause PFK-1.1::EGFP (*cyan*, *middle panel*) to form condensates. Merged image (*bottom panel*) shows colocalization of the CRY2-tagged (*magenta*) and non-CRY2-tagged (*cyan*) PFK-1.1 condensates (*white arrowheads*). (*B*) In transient hypoxic conditions, the fraction of animals displaying a diffuse pattern of RAB-3 in AIY neurons in the wild-type, the loss-of-function allele *pfk-1.1(ola72)* (labeled as *pfk-1.1* mutant), and AIY cell-specific expression of the *pfk-1.1::mCh::CRY2* array in *pfk-1.1(ola72)* animals. Note that the expression of *pfk-1.1::mCh::CRY2* rescues the synaptic vesicle phenotype in *pfk-1.1(ola72)* mutant animals, indicating that *pfk-1.1::mCh::CRY2* is functional. (*C*) Under the same normoxic condition as in (*A*), when coexpressed with mCh::CRY2 (*magenta*, *top panel*), PFK-1.1::EGFP (*cyan*, *middle panel*) remains diffuse. A merged image of the two is shown in the bottom panel. (*D*) A schematic of the localization of PFK-1.1::EGFP in the presence of PFK-1.1::mCh::CRY2 (*top panel*) or control mCh::CRY2. (*E*) PFK-1.1 and ALDO-1 dynamically form clusters in response to a hypoxic condition. Left: formation of PFK-1.1::mRuby-3 (*magenta*) and ALDO-1::EGFP (*green*) condensate (*arrowheads*) through times (*a*)–(*d*). Right: change in the max fluorescence intensity of the PFK-1.1 (*magenta*) and ALDO-1 (*green*) over time. The corresponding four images of (*a*)–(*d*) on the left are indicated with dotted gray lines on the graph. Scale bars, 1 μm. (*F*) PFK-1.1::EGFP condensates in wild-type (*upper image*) and *aldo-1(tm5782)* mutant animals (*lower image*) after 20 min of hypoxia. Arrowheads point at condensates. Note the absence of PFK-1.1 condensates in *aldo-1(tm5782)* mutant animals. (*G*) Same as (*F*), but examining ALDO-1::EGFP in *pfk-1.1 (tm5741)* mutant animals. Note the absence of ALDO-1 condensates in *pfk-1.1(tm5741)* mutant animals. (*A*), (*B*), (*G*), (*H*) scales, 5 μm. (*H*) ALDO-1 (*green*) coexpressed with PFK-1.1::mCh::CRY2 (*magenta*) in normoxic condition (as in *A*). Note CRY2-promoted condensates of PFK-1.1 recruit ALDO-1. Colocalization of the PFK-1.1::CRY2 and ALDO-1 condensates is marked with arrowheads. Scale bars, 2 μm. N = number of animals. Error bars denote SEM. $*p < 0.05$. $**p < 0.01$. $***p < 0.001$ between indicated group.

is recruited into the condensates (Figs. 7 *H* and S7 *C*). Our findings suggest that PFK-1.1 self-association, promoted by the introduction of the CRY2 domain, is capable of recruiting other glycolytic proteins. Together, our findings suggest that PFK-1.1 self-association drives a feed-forward loop that results in the recruitment of other glycolytic proteins and that there is a mutual dependency between glycolytic enzymes for glycolytic protein condensate formation.

DISCUSSION

PFK-1.1 localizes in subcellular compartments in vivo. Although widely regarded as cytosolic in nature, glycolytic enzymes like PFK have long been observed, in both biochemical and immunohistological studies, to self-associate into complexes and be enriched at subcellular compartments in specific cell types (4–13,76). These observations led to the coining of the term "ambiquitous," used to refer to the ability of glycolytic proteins to exist both in soluble and particulate or membrane-bound states (9). Biochemical studies indicated that the state of the glycolytic proteins depended on the metabolic state (and identity) of the tissue from which they were harvested (Wilson (8,9)). The ambiquitous properties of glycolytic proteins, however, remained controversial because the observed biochemical associations were weak, transient, and dependent on the presence of particular metabolites (17,77,78) and because of the lack of supporting in vivo evidence (18). In our study and through a systematic examination of endogenous PFK-1.1 via the use of a hybrid microfluidic-hydrogel device, we conclusively determine that PFK-1.1 indeed displays distinct patterns of subcellular localization in specific tissues in vivo. Our findings are consistent with the hypothesis of the ambiquitous nature of glycolytic enzymes (6,7,9), and with more recent cell biological studies that also observed compartmentalization of glycolytic proteins in response to specific stimuli (14,16,20,79–81).

Our findings on the biophysical properties of PFK-1.1 during transient hypoxia, the fluid-like movements of the condensates, and the correlation of the concentration with the time of emergence indicate that PFK-1.1 clusters represent metastable liquid condensates. The resulting spheroid condensate shapes suggest an interplay between the confinement of the condensate in the neurite's cellular geometry and the surface tension of the condensate. The biophysical properties of PFK-1.1 are different from those observed

for other metabolic enzymes with more static assemblies, such as filamentous structures and crystalline-like assemblies (82). Interestingly, "aged" PFK-1.1 condensates slow down their dynamics, including nonfusing properties, decreased FRAP recovery, and time of dispersion upon normoxia. These findings suggest that changes in the metabolic state of the cell induced by hypoxia result in consistent (and predictable) changes in PFK-1.1 biophysical properties. Our findings also suggest that thermodynamic forces drive phase separation during PFK-1.1 condensation. We note, however, that we also observed in vivo nonequilibrium properties to PFK-1.1 localization that are likely the result of the interplay between cell biological regulatory mechanisms and phase-separated condensates (what have been called "active emulsions" (56)). For example, we observed the exchange of material resulting, not in Ostwald ripening as would be predicted from thermodynamic equilibrium, but instead in similarly sized adjacent condensates. We also observed that the localization of the PFK-1.1 condensates occurred near synapses, where PFK-1.1 was previously shown to be required for sustaining the synaptic vesicle cycle (19). In the muscle, we observed PFK-1.1 is enriched at M-lines and dense body structures, functionally important sites of ATP consumption and muscle contraction (83). Although we have not directly examined the functional implications of phase separation in this study, a recent in vitro study showed that compartmentalization of glycolytic proteins into liquid droplets accelerates the glycolytic reactions (24). Together with our in vivo findings, these observations are consistent with a local "on-demand" assembly of PFK-1.1 condensates, similar to what has been described for other reaction-controlled assemblies of liquid compartments (43,55). Importantly, our findings suggest that thermodynamic driving forces and regulatory biological mechanisms control the ad hoc formation of PFK-1.1 liquid condensates at specific subcellular compartments.

Multivalent interactions in PFK-1.1 are likely important for its condensation. Liquid-liquid phase separation can be induced via regulated multivalent protein-protein and protein-RNA interactions (2,48,61–67). For example, in yeast, cellular redox states regulate the phase separation of ataxin-2, which in turn regulates TORC1 activity in response to the activity state of the mitochondria. Phase separation of ataxin-2 in yeast is regulated via a low complexity domain, composed of a stretch of methionine residues, which mediate protein-RNA interactions (84). Also in yeast, RNA promotes phase separation of glycolytic enzymes during prolongued hypoxia (15,20,85,86). Although we do not find RNA-interacting domains, intrinsically disordered regions, or stretches of methionine residues in PFK-1.1, PFK exists as a homotetramer capable of self-associating into higher-order structures (21). Similar to other self-associating proteins such as hemoglobin, PFK possesses unique geometrical symmetries that result in multivalent interactions that could contribute to phase separation (70–72). Consistent with this model, engineering a CRY2 self-association domain promoted formation of PFK-1.1 condensates. Importantly, induction of PFK-1.1 condensates was sufficient to drive the localization of PFK-1.1 lacking the self-association CRY2 domain and glycolytic protein aldolase/ALDO-1, suggesting that nucleation of PFK-1.1 condensates drive a feed-forward reaction that results in the compartmentalization of glycolytic proteins into condensates. PFK tetramerization and self-association can be regulated by its substrate, by metabolites (including AMP and ATP), and by phosphorylation of its regulatory domain (87). ATP can also act like a biological hydrotrope to solubilize proteins (88). We hypothesize that hypoxic conditions that block the oxidative phosphorylation pathway may result in local changes in concentration of metabolites (such as AMP and ATP), which regulate PFK-1.1 oligomerization states and the local formation of condensates. We note recurring formation of PFK-1.1 condensates at the same location in the neurite. This observation may be reflective of an underlying biology that underpins local metabolite changes or needs. Together, our data are consistent with a model whereby PFK-1.1 oligomerization in response to local metabolites might lead to multivalent interactions that drive its self-association into condensates.

PFK-1.1 condensates might represent a novel glycolytic compartment. The idea that glycolytic proteins compartmentalize into a glycolytic metabolon was first proposed after classical biochemical studies could not explain, based on known biochemical principles, the observed cellular rates of glycolysis (76,89). This led to the hypothesis that higher organizing principles, such as subcellular compartmentalization, must influence the observed flux for the glycolytic metabolic reaction in cells (90,91). Consistent with this, in vitro biochemical studies and modeling have demonstrated that the interaction between PFK and ALDO increases their enzymatic activities (92,93) and that higher-order oligomerization of PFK is associated with an increase in its activity (94). We had previously reported that PFK-1.1 dynamically colocalizes into clusters with other glycolytic proteins, such as aldolase (ALDO) and glyceraldehyde 3-phosphate dehydrogenase (GAPDH) (19). In yeast, prolonged (24-h) hypoxia also results in PFK phase separating with other glycolytic proteins into membraneless subcompartments, termed G-bodies (20,95). In our study, we demonstrate that promoting PFK-1.1 condensates through the use of CRY2 results in recruitment of aldolase to the PFK-1.1 condensates. Observations of glycolytic compartments in multiple different species and cell types suggest that although the regulation, composition, and formation kinetics of the glycolytic condensates may differ, compartmentalization of glycolytic enzymes may be a conserved feature of metabolic organization. We hypothesize that the compartmentalization described here represents a mechanism that changes enzymatic parameters of the kinase to suit changing metabolic needs in the cell. The subcellular organization and biophysical dynamics observed for

PFK-1.1 might extend to other glycolytic proteins, and PFK-1.1 condensates might represent the hypothesized "glycolytic metabolon" (4,6) or a novel membraneless organelle that could regulate glycolysis.

Compartmentalization is a common way for cells to internally organize their reactions and cellular processes (1,22,96,97). Membraneless compartments in cells can serve multiple purposes, from inhibiting enzymatic activity by sequestering molecules to enhancing activity through mass action effects (2,48,97–100). Although metabolic reactions by cytosolic proteins are generally thought of as distributed in cells, emerging evidence suggests that they could be compartmentalized in response to cellular states (15,23,101,102). For example, systematic studies on ~800 metabolic enzymes in yeast identified widespread reorganization of proteins involved in intermediary metabolism upon nutrient starvation (103). Enzymes involved in purine biogenesis are compartmentalized to enhance or inhibit their activity (104,105). Metabolic enzymes such as asparagine synthetase paralogs, CTP synthase, and glucokinase polymerize in response to cellular metabolic changes (106–108). We now show that PFK-1.1 dynamically compartmentalizes into condensates. The principles we uncover here on the subcellular organization of PFK-1.1 could represent important principles underlying the subcellular regulation of glycolysis and conserved concepts on how metabolic processes are dynamically organized to modulate subcellular states.

SUPPORTING MATERIAL

Supporting Material can be found online at https://doi.org/10.1016/j.bpj.2020.08.002.

AUTHOR CONTRIBUTIONS

S.J., Z.X., R.C.L., L.M.J., A.P., D.R.A., A.A.H., and D.A.C.-R. designed research. S.J., Z.X., R.C.L., I.J.G., M.S., S.P., and H.S.K. performed research. S.J., Z.X., and R.C.L. analyzed data. S.J., Z.X., R.C.L., D.R.A., A.A.H., and D.A.C.-R. wrote the manuscript.

ACKNOWLEDGMENTS

We thank Emmanuel Levy and Sucharita Dey (Weizmann Institute), Ceciel Jegers (Hyman lab), Robert Haase and Simon Alberti (MPI-CBG), Ann Cowan (UConn), Leslie Loew (UConn), John Kim and Mindy Clark (Johns Hopkins), Michael Rosen (UT Southwestern), Amy Gladfelter (UNC Chapel Hill), Joseph Hoffman (Yale University), Richard Goodman (Vollum Institute), and members of the Colón-Ramos lab for insightful discussions on the work and advice on the project. We thank the Research Center for Minority Institutions program, the Marine Biological Laboratories, and the Instituto de Neurobiología de la Universidad de Puerto Rico for providing meeting and brainstorming platforms.

Support for S.J. was provided by T32-GM007223. A.A.H., A.P., and L.M.J. were supported by a direct grant from the Max Planck Society. D.R.A. and R.C.L. were supported by National Science Foundation EF1724026 and CBET1605679. Research in the D.A.C.-R. lab was supported by National Institutes of Health R01NS076558 and DP1NS111778 and by an HHMI Scholar Award. The collaboration between D.A.C.-R. lab and A.A.H. is supported by an HFSP Award.

SUPPORTING CITATIONS

References (109,110) appear in the Supporting Material.

REFERENCES

1. Walter, H., and D. E. Brooks. 1995. Phase separation in cytoplasm, due to macromolecular crowding, is the basis for microcompartmentation. *FEBS Lett.* 361:135–139.
2. Banani, S. F., H. O. Lee, …, M. K. Rosen. 2017. Biomolecular condensates: organizers of cellular biochemistry. *Nat. Rev. Mol. Cell Biol.* 18:285–298.
3. Mitrea, D. M., and R. W. Kriwacki. 2016. Phase separation in biology; functional organization of a higher order. *Cell Commun. Signal.* 14:1.
4. Clarke, F. M., and C. J. Masters. 1974. On the association of glycolytic components in skeletal muscle extracts. *Biochim. Biophys. Acta.* 358:193–207.
5. Knull, H. R. 1978. Association of glycolytic enzymes with particulate fractions from nerve endings. *Biochim. Biophys. Acta.* 522:1–9.
6. Kurganov, B. I., N. P. Sugrobova, and L. S. Mil'man. 1985. Supramolecular organization of glycolytic enzymes. *J. Theor. Biol.* 116:509–526.
7. Masters, C. 1984. Interactions between glycolytic enzymes and components of the cytomatrix. *J. Cell Biol.* 99:222s–225s.
8. Wilson, J. E. 1968. Brain hexokinase. A proposed relation between soluble-particulate distribution and activity in vivo. *J. Biol. Chem.* 243:3640–3647.
9. Wilson, J. E. 1978. Ambiquitous enzymes - variation in intracellular-distribution as a regulatory mechanism. *Trends Biochem. Sci.* 3:124–125.
10. Chu, H., E. Puchulu-Campanella, …, J. F. Hoffman. 2012. Identification of cytoskeletal elements enclosing the ATP pools that fuel human red blood cell membrane cation pumps. *Proc. Natl. Acad. Sci. USA.* 109:12794–12799.
11. Green, D. E., E. Murer, …, H. Baum. 1965. Association of integrated metabolic pathways with membranes. I. Glycolytic enzymes of the red blood corpuscle and yeast. *Arch. Biochem. Biophys.* 112:635–647.
12. Mercer, R. W., and P. B. Dunham. 1981. Membrane-bound ATP fuels the Na/K pump. Studies on membrane-bound glycolytic enzymes on inside-out vesicles from human red cell membranes. *J. Gen. Physiol.* 78:547–568.
13. Sullivan, D. T., R. MacIntyre, …, L. Ramizel. 2003. Analysis of glycolytic enzyme co-localization in Drosophila flight muscle. *J. Exp. Biol.* 206:2031–2038.
14. De Bock, K., M. Georgiadou, and P. Carmeliet. 2013. Role of endothelial cell metabolism in vessel sprouting. *Cell Metab.* 18:634–647.
15. Kastritis, P. L., and A.-C. Gavin. 2018. Enzymatic complexes across scales. *Essays Biochem.* 62:501–514.
16. Kohnhorst, C. L., M. Kyoung, …, S. An. 2017. Identification of a multienzyme complex for glucose metabolism in living cells. *J. Biol. Chem.* 292:9191–9203.
17. Brooks, S. P., and K. B. Storey. 1991. Where is the glycolytic complex? A critical evaluation of present data from muscle tissue. *FEBS Lett.* 278:135–138.
18. Menard, L., D. Maughan, and J. Vigoreaux. 2014. The structural and functional coordination of glycolytic enzymes in muscle: evidence of a metabolon? *Biology (Basel).* 3:623–644.
19. Jang, S., J. C. Nelson, …, D. A. Colón-Ramos. 2016. Glycolytic enzymes localize to synapses under energy stress to support synaptic function. *Neuron.* 90:278–291.

20. Jin, M., G. G. Fuller, …, J. K. Kim. 2017. Glycolytic enzymes coalesce in G bodies under hypoxic stress. *Cell Rep.* 20:895–908.
21. Webb, B. A., A. M. Dosey, …, D. L. Barber. 2017. The glycolytic enzyme phosphofructokinase-1 assembles into filaments. *J. Cell Biol.* 216:2305–2313.
22. Wombacher, H. 1983. Molecular compartmentation by enzyme cluster formation. A view over current investigations. *Mol. Cell. Biochem.* 56:155–164.
23. Zecchin, A., P. C. Stapor, …, P. Carmeliet. 2015. Metabolic pathway compartmentalization: an underappreciated opportunity? *Curr. Opin. Biotechnol.* 34:73–81.
24. Ura, T., S. Tomita, and K. Shiraki. 2020. Dynamic formation of liquid droplets triggered by sequential enzymatic reactions. *ChemRxiv* https://doi.org/10.26434/chemrxiv.11930403.v1.
25. Brenner, S. 1974. The genetics of *Caenorhabditis elegans*. *Genetics.* 77:71–94.
26. Lagoy, R. C., and D. R. Albrecht. 2015. Microfluidic devices for behavioral analysis, microscopy, and neuronal imaging in *Caenorhabditis elegans*. *Methods Mol. Biol.* 1327:159–179.
27. Burnett, K., E. Edsinger, and D. R. Albrecht. 2018. Rapid and gentle hydrogel encapsulation of living organisms enables long-term microscopy over multiple hours. *Commun. Biol.* 1:73.
28. Powell-Coffman, J. A. 2010. Hypoxia signaling and resistance in *C. elegans*. *Trends Endocrinol. Metab.* 21:435–440.
29. Brangwynne, C. P., C. R. Eckmann, …, A. A. Hyman. 2009. Germline P granules are liquid droplets that localize by controlled dissolution/condensation. *Science.* 324:1729–1732.
30. Webb, B. A., F. Forouhar, …, D. L. Barber. 2015. Structures of human phosphofructokinase-1 and atomic basis of cancer-associated mutations. *Nature.* 523:111–114.
31. Francis, G. R., and R. H. Waterston. 1985. Muscle organization in *Caenorhabditis elegans*: localization of proteins implicated in thin filament attachment and I-band organization. *J. Cell Biol.* 101:1532–1549.
32. Gieseler, K., H. Qadota, and G. M. Benian. 2017. Development, structure, and maintenance of *C. elegans* body wall muscle. *WormBook.* 2017:1–59.
33. Moerman, D. G., and B. D. Williams. 2006. Sarcomere assembly in *C. elegans* muscle. *WormBook* 1–16.
34. Qadota, H., and G. M. Benian. 2010. Molecular structure of sarcomere-to-membrane attachment at M-Lines in *C. elegans* muscle. *J. Biomed. Biotechnol.* 2010:864749.
35. Dickinson, D. J., A. M. Pani, …, B. Goldstein. 2015. Streamlined genome engineering with a self-excising drug selection cassette. *Genetics.* 200:1035–1049.
36. Flavell, S. W., N. Pokala, …, C. I. Bargmann. 2013. Serotonin and the neuropeptide PDF initiate and extend opposing behavioral states in *C. elegans*. *Cell.* 154:1023–1035.
37. Schwartz, M. L., and E. M. Jorgensen. 2016. SapTrap, a toolkit for high-throughput CRISPR/Cas9 gene modification in *Caenorhabditis elegans*. *Genetics.* 202:1277–1288.
38. Protter, D. S. W., and R. Parker. 2016. Principles and properties of stress granules. *Trends Cell Biol.* 26:668–679.
39. Huelgas-Morales, G., C. G. Silva-García, …, R. E. Navarro. 2016. The stress granule RNA-binding protein TIAR-1 protects female germ cells from heat shock in *Caenorhabditis elegans*. *G3 (Bethesda).* 6:1031–1047.
40. Sun, Y., P. Yang, …, H. Zhang. 2011. A genome-wide RNAi screen identifies genes regulating the formation of P bodies in *C. elegans* and their functions in NMD and RNAi. *Protein Cell.* 2:918–939.
41. Gardner, L. B. 2008. Hypoxic inhibition of nonsense-mediated RNA decay regulates gene expression and the integrated stress response. *Mol. Cell. Biol.* 28:3729–3741.
42. Gottschald, O. R., V. Malec, …, J. Hänze. 2010. TIAR and TIA-1 mRNA-binding proteins co-aggregate under conditions of rapid oxygen decline and extreme hypoxia and suppress the HIF-1α pathway. *J. Mol. Cell Biol.* 2:345–356.
43. Shin, Y., and C. P. Brangwynne. 2017. Liquid phase condensation in cell physiology and disease. *Science.* 357:eaaf4382.
44. Brangwynne, C. P., T. J. Mitchison, and A. A. Hyman. 2011. Active liquid-like behavior of nucleoli determines their size and shape in *Xenopus laevis* oocytes. *Proc. Natl. Acad. Sci. USA.* 108:4334–4339.
45. Franzmann, T. M., M. Jahnel, …, S. Alberti. 2018. Phase separation of a yeast prion protein promotes cellular fitness. *Science.* 359:eaao5654.
46. Patel, A., H. O. Lee, …, S. Alberti. 2015. A liquid-to-solid phase transition of the ALS protein FUS accelerated by disease mutation. *Cell.* 162:1066–1077.
47. Zeng, M., Y. Shang, …, M. Zhang. 2016. Phase transition in postsynaptic densities underlies formation of synaptic complexes and synaptic plasticity. *Cell.* 166:1163–1175.e12.
48. Alberti, S., A. Gladfelter, and T. Mittag. 2019. Considerations and challenges in studying liquid-liquid phase separation and biomolecular condensates. *Cell.* 176:419–434.
49. Gopal, P. P., J. J. Nirschl, …, E. L. F. Holzbaur. 2017. Amyotrophic lateral sclerosis-linked mutations increase the viscosity of liquid-like TDP-43 RNP granules in neurons. *Proc. Natl. Acad. Sci. USA.* 114:E2466–E2475.
50. Xuan, Z., L. Manning, …, P. T. Kurshan. 2017. Clarinet (CLA-1), a novel active zone protein required for synaptic vesicle clustering and release. *eLife.* 6:e29276.
51. Style, R. W., T. Sai, …, E. R. Dufresne. 2018. Liquid-liquid phase separation in an elastic network. *Phys. Rev. X.* 8:011028.
52. Rosowski, K. A., T. Sai, …, E. R. Dufresne. 2020. Elastic ripening and inhibition of liquid-liquid phase separation. *Nat. Phys.* 16:422–425.
53. Zwicker, D., R. Seyboldt, …, F. Jülicher. 2017. Growth and division of active droplets provides a model for protocells. *Nat. Phys.* 13:408–413.
54. Voorhees, P. W. 1992. Ostwald ripening of two-phase mixtures. *Annu. Rev. Mater. Sci.* 22:197–215.
55. Berry, J., C. P. Brangwynne, and M. Haataja. 2018. Physical principles of intracellular organization via active and passive phase transitions. *Rep. Prog. Phys.* 81:046601.
56. Weber, C. A., D. Zwicker, …, C. F. Lee. 2019. Physics of active emulsions. *Rep. Prog. Phys.* 82:064601.
57. Mastro, A. M., M. A. Babich, …, A. D. Keith. 1984. Diffusion of a small molecule in the cytoplasm of mammalian cells. *Proc. Natl. Acad. Sci. USA.* 81:3414–3418.
58. Feric, M., N. Vaidya, …, C. P. Brangwynne. 2016. Coexisting liquid phases underlie nucleolar subcompartments. *Cell.* 165:1686–1697.
59. Hyman, A. A., C. A. Weber, and F. Jülicher. 2014. Liquid-liquid phase separation in biology. *Annu. Rev. Cell Dev. Biol.* 30:39–58.
60. Banani, S. F., A. M. Rice, …, M. K. Rosen. 2016. Compositional control of phase-separated cellular bodies. *Cell.* 166:651–663.
61. Elbaum-Garfinkle, S., Y. Kim, …, C. P. Brangwynne. 2015. The disordered P granule protein LAF-1 drives phase separation into droplets with tunable viscosity and dynamics. *Proc. Natl. Acad. Sci. USA.* 112:7189–7194.
62. Langdon, E. M., Y. Qiu, …, A. S. Gladfelter. 2018. mRNA structure determines specificity of a polyQ-driven phase separation. *Science.* 360:922–927.
63. Li, P., S. Banjade, …, M. K. Rosen. 2012. Phase transitions in the assembly of multivalent signalling proteins. *Nature.* 483:336–340.
64. Nott, T. J., E. Petsalaki, …, A. J. Baldwin. 2015. Phase transition of a disordered nuage protein generates environmentally responsive membraneless organelles. *Mol. Cell.* 57:936–947.
65. Smith, J., D. Calidas, …, G. Seydoux. 2016. Spatial patterning of P granules by RNA-induced phase separation of the intrinsically-disordered protein MEG-3. *eLife.* 5:e21337.
66. Wang, J., J.-M. Choi, …, A. A. Hyman. 2018. A molecular grammar governing the driving forces for phase separation of prion-like RNA binding proteins. *Cell.* 174:688–699.e16.

67. Zhang, H., S. Elbaum-Garfinkle, …, A. S. Gladfelter. 2015. RNA controls PolyQ protein phase transitions. *Mol. Cell.* 60:220–230.

68. Bracha, D., M. T. Walls, …, C. P. Brangwynne. 2018. Mapping local and global liquid phase behavior in living cells using photo-oligomerizable seeds. *Cell.* 175:1467–1480.e13.

69. Shin, Y., J. Berry, …, C. P. Brangwynne. 2017. Spatiotemporal control of intracellular phase transitions using light-activated optoDroplets. *Cell.* 168:159–171.e14.

70. Chen, Q., P. G. Vekilov, …, R. E. Hirsch. 2004. Liquid-liquid phase separation in hemoglobins: distinct aggregation mechanisms of the beta6 mutants. *Biophys. J.* 86:1702–1712.

71. Galkin, O., K. Chen, …, P. G. Vekilov. 2002. Liquid-liquid separation in solutions of normal and sickle cell hemoglobin. *Proc. Natl. Acad. Sci. USA.* 99:8479–8483.

72. Garcia-Seisdedos, H., C. Empereur-Mot, …, E. D. Levy. 2017. Proteins evolve on the edge of supramolecular self-assembly. *Nature.* 548:244–247.

73. Bugaj, L. J., A. T. Choksi, …, D. V. Schaffer. 2013. Optogenetic protein clustering and signaling activation in mammalian cells. *Nat. Methods.* 10:249–252.

74. Che, D. L., L. Duan, …, B. Cui. 2015. The dual characteristics of light-induced cryptochrome 2, homo-oligomerization and heterodimerization, for optogenetic manipulation in mammalian cells. *ACS Synth. Biol.* 4:1124–1135.

75. Park, H., N. Y. Kim, …, W. D. Heo. 2017. Optogenetic protein clustering through fluorescent protein tagging and extension of CRY2. *Nat. Commun.* 8:30.

76. Moses, V. 1978. Mechanism for the intracellular compartmentation of newly synthesized proteins. *In* Microenvironments and Metabolic Compartmentation. P. A. Srere and R. W. Estabrook, eds. Academic Press, pp. 169–185.

77. Vas, M., and J. Batke. 1981. Evidence for absence of an interaction between purified 3-phosphoglycerate kinase and glyceraldehyde-3-phosphate dehydrogenase. *Biochim. Biophys. Acta.* 660:193–198.

78. Weber, J. P., and S. A. Bernhard. 1982. Transfer of 1,3-diphosphoglycerate between glyceraldehyde-3-phosphate dehydrogenase and 3-phosphoglycerate kinase via an enzyme-substrate-enzyme complex. *Biochemistry.* 21:4189–4194.

79. Araiza-Olivera, D., N. Chiquete-Felix, …, S. Uribe-Carvajal. 2013. A glycolytic metabolon in *Saccharomyces cerevisiae* is stabilized by F-actin. *FEBS J.* 280:3887–3905.

80. Graham, J. W. A., T. C. R. Williams, …, L. J. Sweetlove. 2007. Glycolytic enzymes associate dynamically with mitochondria in response to respiratory demand and support substrate channeling. *Plant Cell.* 19:3723–3738.

81. Miura, N., M. Shinohara, …, M. Ueda. 2013. Spatial reorganization of *Saccharomyces cerevisiae* enolase to alter carbon metabolism under hypoxia. *Eukaryot. Cell.* 12:1106–1119.

82. Petrovska, I., E. Nüske, …, S. Alberti. 2014. Filament formation by metabolic enzymes is a specific adaptation to an advanced state of cellular starvation. *eLife.* 3:e02409.

83. Wojtas, K., N. Slepecky, …, D. Sullivan. 1997. Flight muscle function in Drosophila requires colocalization of glycolytic enzymes. *Mol. Biol. Cell.* 8:1665–1675.

84. Kato, M., Y.-S. Yang, …, B. P. Tu. 2019. Redox state controls phase separation of the yeast ataxin-2 protein via reversible oxidation of its methionine-rich low-complexity domain. *Cell.* 177:711–721.e8.

85. Castello, A., B. Fischer, …, M. W. Hentze. 2016. Comprehensive identification of RNA-binding domains in human cells. *Mol. Cell.* 63:696–710.

86. Mazurek, S., F. Hugo, …, E. Eigenbrodt. 1996. Studies on associations of glycolytic and glutaminolytic enzymes in MCF-7 cells: role of P36. *J. Cell. Physiol.* 167:238–250.

87. Sola-Penna, M., D. Da Silva, …, P. Zancan. 2010. Regulation of mammalian muscle type 6-phosphofructo-1-kinase and its implication for the control of the metabolism. *IUBMB Life.* 62:791–796.

88. Patel, A., L. Malinovska, …, A. A. Hyman. 2017. ATP as a biological hydrotrope. *Science.* 356:753–756.

89. Sies, H. 1982. Metabolic Compartmentation. Academic Press, Cambridge, MA.

90. Cori, C. F. 1956. Problems of cellular biochemistry. *In* Currents in Biochemical Research. D. E. Green, ed. Interscience, pp. 198–214.

91. Srere, P. A., and K. Mosbach. 1974. Metabolic compartmentation: symbiotic, organellar, multienzymic, and microenvironmental. *Annu. Rev. Microbiol.* 28:61–83.

92. Marcondes, M. C., M. Sola-Penna, …, P. Zancan. 2011. Muscle-type 6-phosphofructo-1-kinase and aldolase associate conferring catalytic advantages for both enzymes. *IUBMB Life.* 63:435–445.

93. Raïs, B., F. Ortega, …, M. Cascante. 2000. Quantitative characterization of homo- and heteroassociations of muscle phosphofructokinase with aldolase. *Biochim. Biophys. Acta.* 1479:303–314.

94. Su, J. Y., and K. B. Storey. 1995. Fish muscle phosphofructokinase - influences of protein-concentration on enzyme-kinetic behavior. *Int. J. Biochem. Cell Biol.* 27:1277–1283.

95. Fuller, G. G., T. Han, …, J. K. Kim. 2020. RNA promotes phase separation of glycolysis enzymes into yeast G bodies in hypoxia. *eLife.* 9:e48480.

96. Alberti, S. 2017. Phase separation in biology. *Curr. Biol.* 27:R1097–R1102.

97. Schmitt, D. L., and S. An. 2017. Spatial organization of metabolic enzyme complexes in cells. *Biochemistry.* 56:3184–3196.

98. Case, L. B., X. Zhang, …, M. K. Rosen. 2019. Stoichiometry controls activity of phase-separated clusters of actin signaling proteins. *Science.* 363:1093–1097.

99. Lee, C., H. Zhang, …, A. S. Gladfelter. 2013. Protein aggregation behavior regulates cyclin transcript localization and cell-cycle control. *Dev. Cell.* 25:572–584.

100. Su, X., J. A. Ditlev, …, R. D. Vale. 2016. Phase separation of signaling molecules promotes T cell receptor signal transduction. *Science.* 352:595–599.

101. O'Connell, J. D., A. Zhao, …, E. M. Marcotte. 2012. Dynamic reorganization of metabolic enzymes into intracellular bodies. *Annu. Rev. Cell Dev. Biol.* 28:89–111.

102. Prouteau, M., and R. Loewith. 2018. Regulation of cellular metabolism through phase separation of enzymes. *Biomolecules.* 8:160.

103. Narayanaswamy, R., M. Levy, …, E. M. Marcotte. 2009. Widespread reorganization of metabolic enzymes into reversible assemblies upon nutrient starvation. *Proc. Natl. Acad. Sci. USA.* 106:10147–10152.

104. An, S., R. Kumar, …, S. J. Benkovic. 2008. Reversible compartmentalization of de novo purine biosynthetic complexes in living cells. *Science.* 320:103–106.

105. Pedley, A. M., and S. J. Benkovic. 2017. A new view into the regulation of purine metabolism: the purinosome. *Trends Biochem. Sci.* 42:141–154.

106. Noree, C., E. Monfort, …, J. E. Wilhelm. 2014. Common regulatory control of CTP synthase enzyme activity and filament formation. *Mol. Biol. Cell.* 25:2282–2290.

107. Noree, C., N. Sirinonthanawech, and J. E. Wilhelm. 2019. *Saccharomyces cerevisiae* ASN1 and ASN2 are asparagine synthetase paralogs that have diverged in their ability to polymerize in response to nutrient stress. *Sci. Rep.* 9:278.

108. Stoddard, P. R., E. M. Lynch, …, E. C. Garner. 2019. Independent evolution of polymerization in the Actin ATPase clan regulates hexokinase activity. *bioRxiv* https://doi.org/10.1101/686915.

109. Mello, C., and A. Fire. 1995. DNA transformation. *Methods Cell Biol.* 48:451–482.

110. Thévenaz, P., U. E. Ruttimann, and M. Unser. 1998. A pyramid approach to subpixel registration based on intensity. *IEEE Trans. Image Process.* 7:27–41.

Biophysical Journal, Volume *120*

Supplemental information

Phosphofructokinase relocalizes into subcellular compartments with liquid-like properties in vivo

SoRi Jang, Zhao Xuan, Ross C. Lagoy, Louise M. Jawerth, Ian J. Gonzalez, Milind Singh, Shavanie Prashad, Hee Soo Kim, Avinash Patel, Dirk R. Albrecht, Anthony A. Hyman, and Daniel A. Colón-Ramos

Supplementary Methods

C. elegans strains and transgenic lines

For C-terminal endogenous tagging of PFK-1.1, a cell-specific CRISPR protocol (1, 2) was used to insert two flippase recombinase target (FRT) sites flanking *let-858* 3'-UTR that contains a transcriptional stop motif followed by a GFP sequence in front of the endogenous *pfk-1.1* 3'-UTR in the X chromosome (*pfk-1.1(ola368)*). Upon injection of cell-specific transgenes expressing FLPase, the *let-858* 3'-UTR containing the transcriptional stop motif is excised, leaving GFP fused to the C-terminus of PFK-1.1. To achieve specific expression of PFK-1.1::GFP in neurons and the body wall muscle, *unc-47* and *mig-13* promoters were used to drive the expression of FLPase in those cells.

For generating expression clones, Gateway system (Invitrogen) and Gibson system (New England Biolabs) were primarily used. Transgenic strains (0.5–30 ng/µl) were made using standard techniques (3) and coinjected with markers *Punc-122::gfp, Punc-122::rfp, or Podr-1::rfp*. See Table 1 for all strains used in this study.

Supplementary Table 1. Strains used in this study

Strain Name	Genotype
DCR7312	*olaex4409 [Ppfk-1.1:: pfk-1.1::egfp]*
DCR6732	*pfk-1.1(ola368)[pfk-1.1::FLP-ON::gfp]; olaex4038 [Pmig-13::FLPase]*
DCR6941	*pfk-1.1(ola368)[pfk-1.1::FLP-ON::gfp]; olaex4140 [Punc-47::FLPase]*
DCR6037	*olaex3534 [Punc-47::pfk-1.1::egfp; Punc-47::snb-1::mCherry]*
DCR7155	*olaex4296 [Punc-47::pfk-1.1::mRuby-3; Punc-47::tiar-1a::egfp]*
DCR7151	*olaex4292 [Pttx-3::sl2::pfk-1.1::mRuby-3; Pttx-3::sl2::tiar-1a::egfp]*
DCR3921	*olaex2271 [Punc-47::pfk-1.1::egfp; Punc-47::tom-20::mCherry]*
DCR7799	*olaex4731 [Pttx3::sl2::pfk-1.1::mCh::cry2; Pttx3::sl2::pfk-1.1::egfp]*
DCR7801	*olaex4733 [Pttx3::sl2::mCh::cry2; Pttx3::sl2::pfk-1.1::egfp]*
DCR6426	*olaex3802 [Punc-47::pfk-1.1::egfp; Punc-47::mCherry]*
TV1449	*WyEx505 [Pttx-3::mCherry::erc; Pttx-3::gfp::rab-3]*
DCR1564	*pfk-1.1 (ola72); WyEx505*

DCR6987	*olaex4180 [Pttx-3::gfp::rab-3; Pttx-3::pfk-1.1::mCherry::cry2]; pfk-1.1 (ola72)*
DCR6909	*olaex4123 [Pttx-3::sl2::aldo-1::egfp; Pttx-3::sl2::pfk-1.1::mCh::cry2]*
DCR6445	*olaex3818 [Punc-47::pfk-1.1::egfp::cry2; Punc-47::snb-1::mCh]*
DCR7122	*olaex4276 [Pttx-3::sl2::aldo-1::egfp]*
DCR7124	*pfk-1.1(tm5741); olaex4276*
DCR4761	*olaIs39 [Pttx-3::sl2::pfk-1.1::egfp; Pttx-3::mCh::rab-3]*
DCR7006	*olaIs39; aldo-1(tm5782)*
DCR6094	*olaex3582 [Punc-47::aldo-1::egfp; Punc-47::pfk-1.1::mRuby-3]*

Hybrid microfluidic-hydrogel device set-up and calibration

A reusable microfluidic PDMS device was fabricated to deliver gases through a channel adjacent to immobilized animals, following protocols as previously described (4). A 50 µm, oxygen-permeable PDMS membrane was permanently bonded using air plasma to create an enclosed arena for gas flow, while the opposite side of the device was permanently bonded to a glass slide for structural integrity. Right-angle inlet and outlet holes were punched in the PDMS for ease of use with high-magnification inverted and upright microscopes. This reusable assembly was cleaned before each use by wiping the PDMS surface with ethanol, drying, and removing any remaining dust with tape. Animals were kept stationary during high-resolution imaging and exposure to shifting gas concentrations at the membrane surface by hydrogel immobilization (5). To prepare the hydrogel assembly, a small volume (2 µL) of gel (20% PEGDA and 0.05% Irgacure 2959 in water) was pipetted onto the center of a hydrophobic glass slide containing a 100 µm thick PDMS spacer with a 6 mm diameter hole in the center, forming a rounded gel droplet. Glass slides or coverslips were rendered hydrophobic by 1 hour exposure to (tridecafluoro-1,1,2,2-tetrahydrooctyl) trichlorosilane vapor in a vacuum chamber, or “gel-adhesive” by 3 min exposure to 5% 3-(trimethoxysilyl)propyl methacrylate in ethanol (5), which covalently grafts methacrylate groups to the glass that in turn covalently bind to the PEG chains of the hydrogel. Animals were then transferred into the solution and a gel-adhesive coverslip was placed over the hydrogel drop supported by the spacer. The assembly was

placed over a UV light source (UVP, model UVGL-15, 4W) and illuminated for 2 minutes at 365 nm for gelation. The coverslip with spacer was carefully lifted off of the hydrophobic slide and a 2 µL drop of muscimol (50 mM in water) was then pipetted directly over the hydrogel disk. The gas device was carefully centered and lowered on top of the hydrogel assembly and clamped into a P2 series holder (Warner Instruments) to complete the closed system. Lastly, microfluidic tubing and components were connected to a nitrogen tank set to approximately 1-10 psi using a low-pressure regulator. To generate hypoxic conditions in the hydrogel, nitrogen flow was delivered continuously through the device assembly and confirmed by observing bubbles in a waste beaker filled with water connected with tubing to the device outlet. To generate normoxic conditions in the hydrogel, the nitrogen tank was turned off and the inlet tubing was immediately disconnected at the tank. Note that, in addition to the 0% oxygen condition, we also repeated the hypoxic experiments using 8% oxygen condition in the same setup and obtained similar results (data not shown). *C. elegans* can survive anoxic condition for a whole day (6), and for our hypoxic experiments, which ranged from minutes to an hour, the animals were rescued and shown to be viable post transient hypoxia.

For device calibration, oxygen dynamics within the hydrogel were monitored by adding 4 µL of an oxygen sensitive fluorescent dye solution, 0.75 mM $Ru(phen)_3Cl_2$ dissolved in water, onto a 2 µL hydrogel disk before assembling with the gas device. Also, an oxygen probe (Ocean Optics HIOXY-PI600) was plugged into a second outlet to monitor corresponding oxygen concentration levels in the gas channel. A two-way solenoid pinch valve (NResearch 161P091) and custom Arduino controller were used to switch between constant flows of nitrogen or air (21% oxygen) through the device via separate inlets (Fig. S2 A). After this initial set-up, the oxygen probe was calibrated using a two-point calibration during nitrogen (0% oxygen) and air (21% oxygen) flow. MicroManager software was used to configure camera (2x2 binning and 1 second exposure) and acquisition settings (1 frame per second) for monitoring changes in fluorescence intensity

through a 10X Leica objective (0.4 NA), RFP single-band filter set, detected by a Hammamatsu ORCA-ER mounted on a Leica DMI6000B microscope with EXFO X-Cite 120 Fluorescence Illumination System. A sequence of valve switches and tubing change steps were used to control shifts in oxygen concentration and monitored at 1 sample per second with the probe while synchronously recording changes in $Ru(phen)_3Cl_2$ hydrogel intensity (Fig. S2 B). This sequence was saved as a single TIFF stack file and repeated without disturbing the set-up and field of view for a second calibration trial. Mean fluorescence over the full field-of-view (672 x 512 px) centered on the hydrogel disk was measured for all 1200 frames and synchronized with oxygen concentration measurements from the outlet probe in the gas channel. Normalized fluorescence was calculated by scaling between the minimum fluorescence during steady 21% oxygen and the maximum fluorescence at steady 0% oxygen (as fluorescence scales inversely with oxygen). Slight increases in both minimum and maximum fluorescence of the oxygen sensor in the hydrogel were observed over time, likely due to a slow increase in concentration of the oxygen sensitive dye from evaporation. Scaling was adjusted by a linear interpolation of fluorescence envelope between the 0 – 21% oxygen transitions at minute 1 and near minute 15 (Fig. S2 B). To determine the calibration curve between hydrogel fluorescence and oxygen concentration, normalized fluorescence values were plotted against gas channel oxygen measurements, excluding data at times just following valve switches where hydrogel and gas channel concentrations would not be equal due to oxygen diffusion delays. The median fluorescence at binned oxygen concentration values (0.5% O_2 bins) revealed a non-linear relationship between measured oxygen percent and fluorescence in the hydrogel (Fig. S2 C). This calibration curve was used to estimate oxygen concentration in the hydrogel based on linear interpolation between binned values (Fig. S2 D). From this, we estimate that switching between 21% and 0% oxygen in the hydrogel requires about 30 seconds to 1 minute, while switching between 0% and 21% oxygen in the hydrogel is nearly immediate. The directional difference in switching dynamics is likely due to the high oxygen concentration in PDMS (with

high gas permeability) from ambient air, making it faster to increase oxygen, although hysteresis in dye fluorescence or kinetics could also contribute. All analysis was completed using MATLAB R2017a.

Microscopy and image processing

Images of fluorescently tagged fusion proteins were captured live in *C. elegans* nematodes using a 60 CFI Plan Apo VC, numerical aperture 1.4, oil-immersion objective on an UltraView VoX spinning-disc confocal microscope (PerkinElmer Life and Analytical Sciences). Worms were immobilized using 50mM muscimol (Abcam) and hydrogel encapsulation (5). ImageJ was used for image analysis, and it was used to adjust for brightness and contrast for image presentation. All the adjustments were kept identical for direct image comparisons unless otherwise stated. Maximum projections were used for all the confocal images, with the exception of the partial fluorescence recovery photobleaching (FRAP) experiments, which were in single planes. To correct for motion movement of the animal in time-lapse images, acquired image slices were mostly aligned using the Stack registration plugin (7) in ImageJ or manually aligned and then the slices concatenated. Rendering of puncta was performed using Amira visualization software (Thermo Fisher Scientific), where gray values were used to create an isosurface superimposed on a gray-scale representation of the puncta in 3D (see Fig. 4 C). Finally, zoomed insets of images were obtained on ImageJ using the “Zoom in Images and Stacks” plugin developed by Gilles Carpentier.

Quantification of phenotypic penetrance of glycolytic protein clustering and diffuse distribution of synaptic vesicle proteins

Animals were scored as displaying either “punctate” or “diffuse” phenotypes for the fluorophore-tagged glycolytic proteins or synaptic vesicle proteins after specified manipulations. Leica DM500B compound fluorescent microscope was used for the scoring. For hypoxia-induced

conditions, coverslip-induced hypoxia was used as previously described (8) to calculate the percentage of animals displaying PFK-1.1 clusters or diffuse distribution of synaptic vesicle proteins. Statistical analyses were performed with Prism (GraphPad) and p values were calculated using Fisher's exact test.

Examination of subcellular localization of PFK-1.1 and stress granule protein TIAR-1

For heat shock induction, animals on NGM plates seeded with OP50 *Escherichia coli*, were incubated at 37°C for 1hour and were imaged immediately after that as previously described (9, 10). For hypoxia induction, coverslip-induced hypoxia was used as previously described (8). AIY and GABAergic neurons were examined.

Quantifications of subcellular localization of fluorophore-tagged proteins

For still images, the subcellular localization of fluorophore-tagged proteins, including PFK-1.1, were quantified using ImageJ and graphs plotted using Prism (GraphPad). 1) For the distribution of fluorophore-tagged proteins along the neurite, segmented line scans were performed and the graph of fluorescence intensity over distance was plotted. 2) In comparing the total amount of fluorophore-tagged proteins found in the neurite before and after hypoxia, an identical ROI around the neurite was drawn for those two time points. Total fluorescence values were obtained by multiplying the ROI with the mean fluorescence values found in the designated region. Finally, to account for any photobleaching, the raw total fluorescence value was normalized to the percent change of the background.

For time-lapse images, 1) a small ROI encapsulating individual area of the neurite where glycolytic clusters appear was designated in ImageJ and max fluorescence value, or pixel intensity, measured for each time point. The measured max fluorescence value was then plotted against time to show its change over time. 2) A segmented line was drawn through the

neurite and kymograph was generated to show how PFK-1.1 protein localization changes under transient hypoxia using ImageJ. All the images used in the quantification analyses were obtained using identical microscopy settings.

Normalization of max fluorescence

To compare how the max fluorescence changes after repetition of hypoxic and normoxic conditions, we normalized the max fluorescence of individual PFK-1.1 punctum at different time points. First, we identified the PFK-1.1 puncta that repeatedly appeared after the first and second round of hypoxic treatment (10 minutes of hypoxia). Then we measured the max fluorescence of individual punctum and the corresponding region for before hypoxia, after 10 minutes of hypoxia, and after an additional five minutes of normoxia. To account for photobleaching, we used a region that did not have PFK-1.1 puncta formation or localization change to normalize for each max fluorescence value. This value was then further normalized to the starting value or before hypoxic treatment to show the fold changes in max fluorescence through hypoxia and normoxia. *p values* comparing the max fluorescence at different time points were calculated using the Mann-Whitney *U* test.

Neurite diameter measurement

To measure the diameter of the neurite, strains expressing cytosolic mCherry in GABAergic neurons were used. Total of 20 measurements was made by measuring the thickness of the fluorescent signal in the GABAergic neurites. Given the varicosity of the neurite, 10 total measurements were made in the synaptic bouton (mean average of 0.83 μm) and the other 10 measurements were made in the non-bouton areas (mean average of 0.45 μm). Total average was calculated by combining all 20 measurements. We also calculated the neurite diameter from GABAergic electron microscopy images in (11).

PFK-1.1 condensate reversal time measurement

The time (in minutes) it takes for PFK-1.1 in its condensate form to disperse in the cytosol was measured and compared between PFK-1.1 condensates that formed after 10 minutes of transient hypoxia and 40 minutes of prolonged hypoxia. To detect the time for the PFK-1.1 condensate to fully disperse, time-lapse images were acquired from the beginning of the hypoxic treatment to up to 30 minutes of normoxic conditions. A condensate was considered as dispersed in the cytosol when the condensate was no longer distinguishable from the background cytoplasmic signal and loss of the spherical shape.

Supplementary Video Legends

Video S1. PFK-1.1 condensates induced by transient hypoxia reverts back to diffuse localization when the condition is returned to normoxia. Transient hypoxia initiates at time 01:20 (minute:second), and also indicated by the appearance of the green square on the top right corner. Hypoxia is terminated 20 minutes later at 21:20. PFK-1.1 condensates can be seen dispersing after 21:20. See also Fig. 3 E. Scale, 5 μm.

Video S2. **PFK-1.1 condensates repeatedly form and disperse during hypoxia-normoxia cycles.** Two rounds of 10 minutes of transient hypoxia (indicated by the appearance of a green square on the top right corner) interspaced with 5 minutes of normoxia are shown. A small region (white outlined box) of the neurite is zoomed in (2x; yellow outlined box) and the outline of PFK-1.1 localization in the same small region is shown on the bottom left corner. Elapsed time is shown in minute:second. See also Fig. 3 F. Scale, 5 μm.

Video S3. PFK-1.1 condensates undergo fusion. The two PFK-1.1 condensates (in the white outlined box) can be seen fusing and relaxing into a spherical shape. A 2x zoomed inset is shown above. Elapsed time is shown in minute:second on the top left corner. Here, 00:00 is post 8 minutes of transient hypoxia. See also Fig. 4 C. Scale, 2 μm.

Video S4. PFK-1.1 condensates exchange material and undergo fusion. The first PFK-1.1 condensate appear around 12 minutes into hypoxia (elapsed time shown as “minute:second” on the top left corner). Another one appears immediately to the right of it around 15 minutes post hypoxia, and the fluorescence intensity between the two condensates fluctuates until around 32 minutes post hypoxia, which then ends with a fusion event. See also Fig. S5 A. Scale, 2 μm.

Video S5. PFK-1.1 condensates exchange materials. Four PFK-1.1 condensates appear in the white boxed region during transient-hypoxia as indicated by the elapsed time on the top left corner in minute:second. 2x zoomed in inset is shown immediately below. The condensates demonstrate fluctuation in fluorescence intensity, suggesting material exchange between the neighboring condensates. See also Fig. 4 E and F. Scale, 2 μm.

Video S6. PFK-1.1 condensates do not all fuse, but do have fluid-like movements. Elapsed time is shown in minute:second on the top left corner. Here, 00:00 is post 30 minutes of prolonged hypoxia. PFK-1.1 condensates in the white boxed region, instead of fusing, “bounce” of each other. Note that compared to the fusion event (shown in Fig. 4 C and Video S3), which happened after approximately 10 minutes into transient hypoxia, the event recorded here is post 30 minutes of prolonged hypoxia. A 2x zoomed inset is shown at the bottom left. See also Fig. S6 B. Scale, 2 μm.

Video S7. PFK-1.1 clusters asynchronously appear in response to transient hypoxia. Hypoxic condition, which is indicated by the appearance of a green square on the top right, starts at time 00:00 (minute:second). See also Fig. 6A. Scale, 5 μm.

Video S8. PFK-1.1 and ALDO-1 dynamically relocalize into condensates under hypoxia. PFK-1.1::mRuby-3 and ALDO-1::EGFP were co-expressed in GABAergic neuron. Three panels shown, from the left, PFK-1.1 (magenta), ALDO-1 (green), and a merge of the two channels (white). Hypoxic condition, which is indicated by the appearance of a green square on the top right, starts at time 00:00. In the middle of the neurite shown here, there is an appearance of a condensate for PFK-1.1 and ALDO-1 around 10 minutes post-hypoxia, which separates into two condensates by ~23 minutes post-hypoxia. Scale bar, 2um.

Supplementary Figures

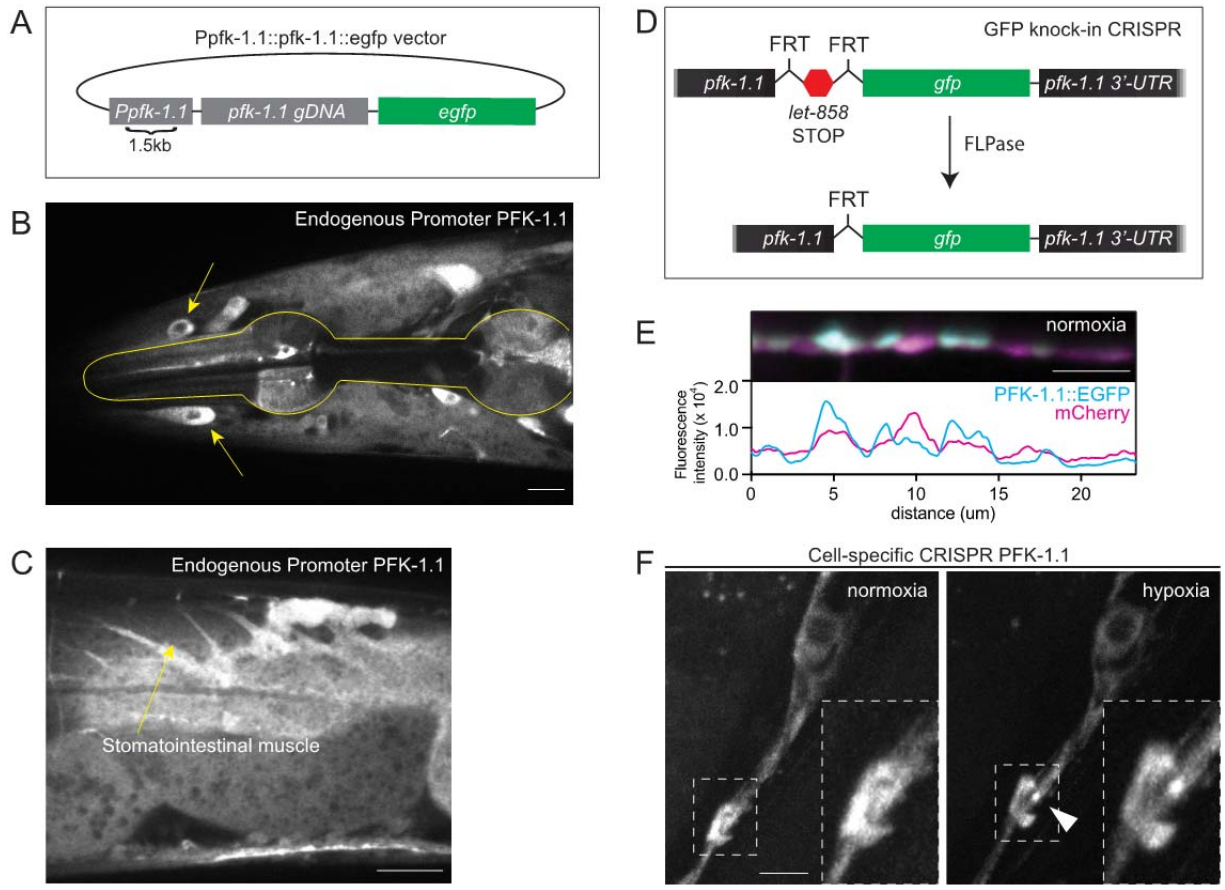

Figure S1. Expression and subcellular localization of PFK-1.1. (**A**) Schematic of the expression vector for PFK-1.1:EGFP driven by its own promoter (Ppfk-1.1:PFK-1.1::EGFP). *Ppfk-1.1* contains 1.5 kilobase (kb) region upstream of the *pfk-1.1* start codon. *pfk-1.1 gDNA* is the genomic sequence of *pfk-1.1* that contains both introns and exons. (**B**) Head of *C. elegans* expressing the *Ppkf-1.1::pfk-1.1::egfp* array. Expression of PFK-1.1 can be seen in the pharyngeal muscle, as outlined, and in other unidentified cells (arrow). Scale, 10 μm. (**C**) Near the tail region of the animal, PFK-1.1 expression is observed in the stomatointestinal muscle.

Scale, 15 μm. (**D**) Schematic of the strategy used for tissue-specific tagging of endogenous PFK-1.1 via conditional CRISPR. (**E**) Cytosolic mCherry (magenta) co-expressed with PFK-1.1 (cyan) in GABAergic neurons to observe the relative distribution of PFK-1.1. Note uneven enrichment of PFK-1.1 through different subcellular neuronal regions even in normoxic conditions. Line scan for PFK-1.1 and mCherry fluorescence level in lower panel. Scale, 5 μm. (**F**) The *unc-47* promoter was used in conditional CRISPR lines to tag the endogenous PFK-1.1 with GFP in a subset of tissues. After 30 minutes of hypoxia, PFK-1.1 clusters can be seen (arrowhead, right panel). Scale, 5 μm.

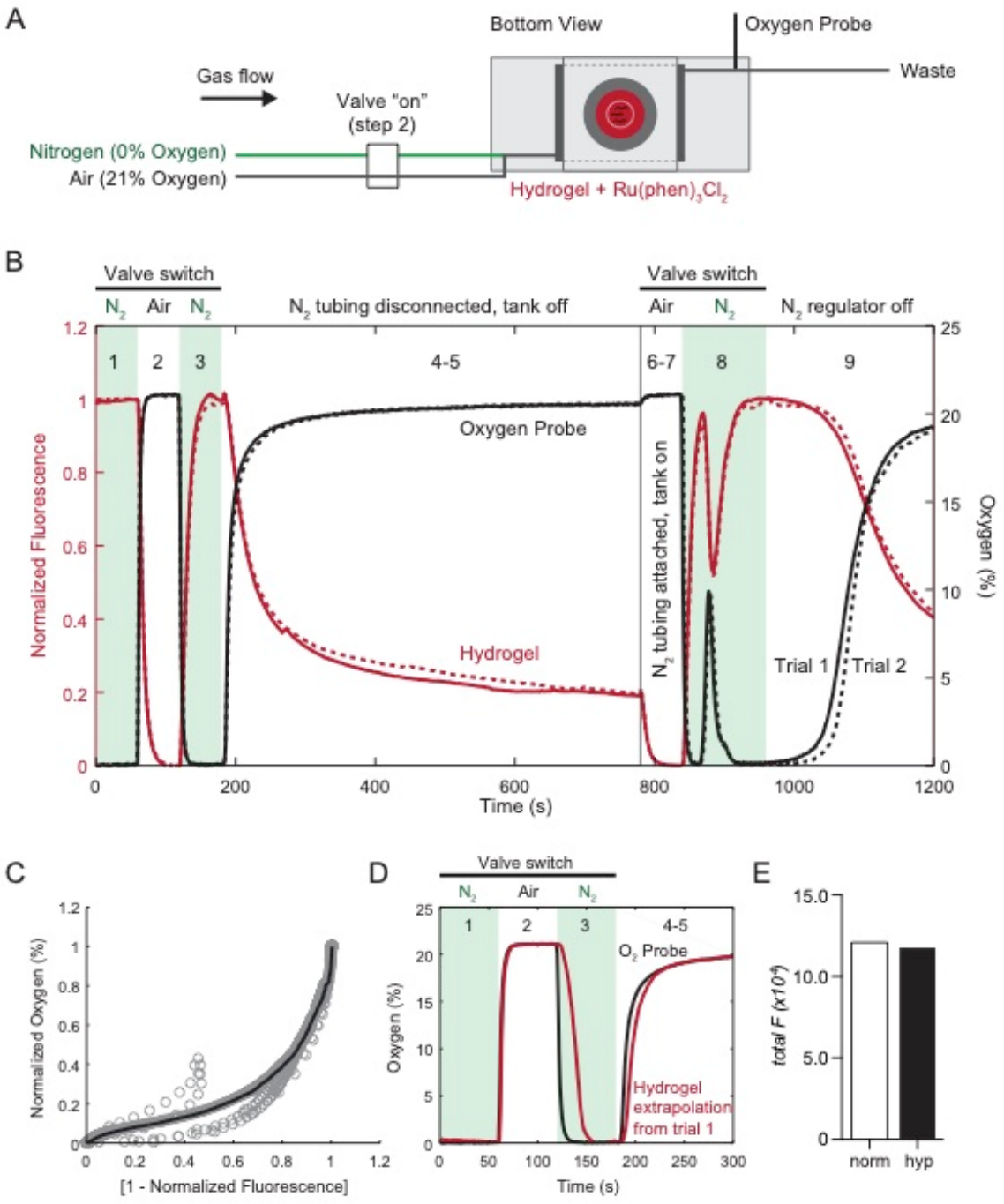

Figure S2. Hybrid microfluidic-hydrogel device and its validation analysis. (**A**) Schematic of hybrid microfluidic-hydrogel device set up for calibration experiments. A pinch valve was used to control flow from compressed nitrogen and air tanks. When the valve was powered "on" using a custom Arduino microcontroller, air flowed through the chamber to the hydrogel and outlet

(shown), in which oxygen concentration levels were continuously monitored using an oxygen probe. Synchronous changes in $Ru(phen)_3Cl_2$ fluorescence were monitored in the hydrogel by epifluorescence microscopy. When the valve was not powered, nitrogen flowed through the chamber (hypoxia) and outlet. (**B**) Line plot of synchronized oxygen probe and epifluorescence microscopy measurements (of $Ru(phen)_3Cl_2$ fluorescence) during a semi-automated sequence of valve switches. First, three valve-controlled switches from (1) nitrogen to (2) air to (3) nitrogen were delivered to observe steady-state minimum and maximum fluorescence intensities, followed by (4) manually turning off the nitrogen tank and (5) immediately disconnecting the nitrogen inlet tubing from the tank for 10 minutes. Next, a valve switch allowed (6) air flow to enter the device to determine shifts in baseline fluorescence. During this time, the nitrogen tubing was (7) re-attached and the tank was turned back on. Another valve switch (8) was used to restore low oxygen levels, yielding a short increase in oxygen likely due to air entering the previously disconnected nitrogen tubing. Finally, to compare differences in switching delays, the nitrogen regulator was (9) turned off and immediately back on after completing the 1200 second acquisition. The exact sequence was executed for a second trial (dashed line) and shown. (**C**) Scatter plot of all normalized oxygen concentrations larger than normalized fluorescence values versus [1 – normalized fluorescence]. Trend line represents the median values of binned oxygen concentration values, with linear interpolation between bins. (**D**) Estimated oxygen concentration in the hydrogel (using the calibration curve in **C**) compared with measured oxygen concentration in the gas channel for the first 300 s in B. (**E**) Total fluorescence of PFK-1.1 in Fig. 2 D neurite for normoxic condition (white box, “norm”) and transiently hypoxic conditions (black box, “hyp”). Note that there are no significant changes in the total levels of neurite fluorescence between the two conditions.

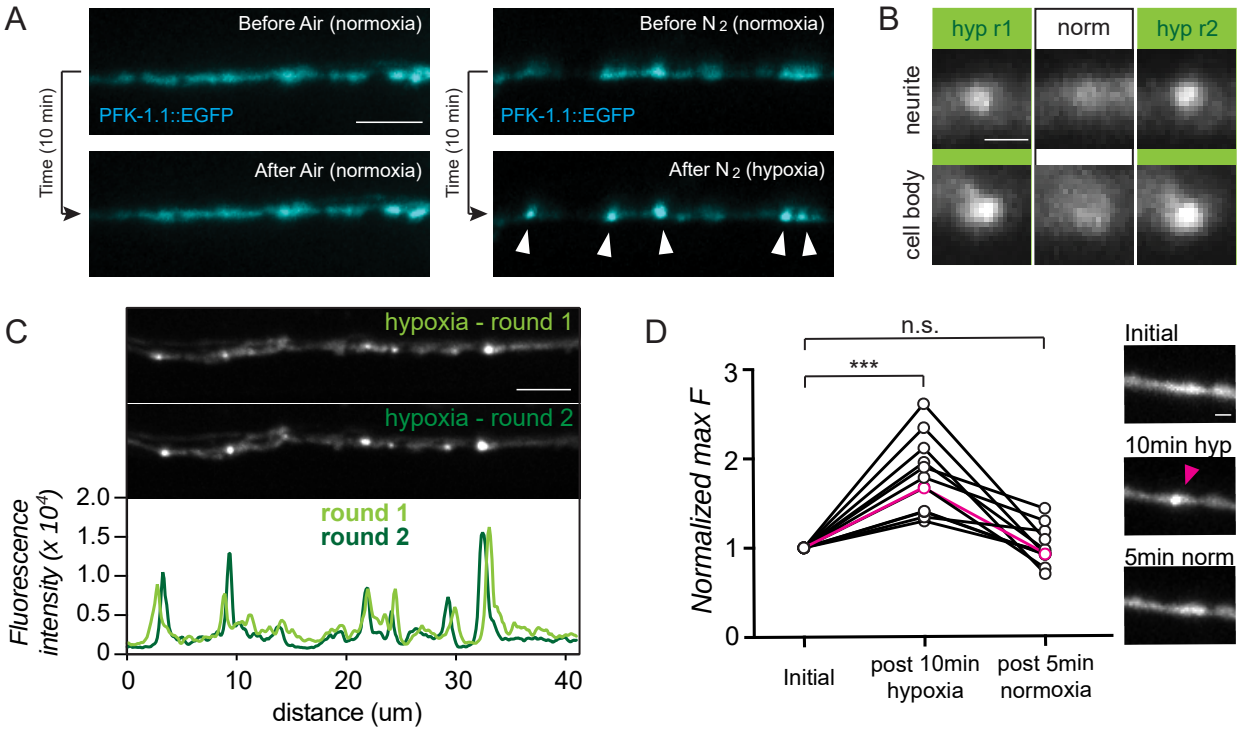

Figure S3. Reversibility of PFK-1.1 condensates. (**A**) PFK-1.1::EGFP before gas treatment (top panels) and after exposure to gas treatment for 10 minutes (bottom panels) with either normal air (left panels) or nitrogen gas (right panels). PFK-1.1 condensates (arrowheads) form specifically in response to transient hypoxic conditions. Scale, 5 μm. (**B**) PFK-1.1 condensates repeatedly appear in both the neurites (top panels) and cell bodies (bottom panels) of neurons through two rounds (r1 and r2) of normoxia ("norm") and transient hypoxia ("hyp") cycles. Scale, 1 μm. (**C**) PFK-1.1 localization after the first round of transient hypoxia (top panel) and the second round of transient hypoxia (middle panel). Note how PFK-1.1 condensates reappear at similar locations (this is another example of an additional neurite, as in Fig. 2 F, G). In lower panel, corresponding line scan for each round of transient hypoxia are shown: first round (light green) and second round (dark green). Scale, 5 μm. (**D**) Calculation of the normalized maximum fluorescence of twelve different neurite regions where PFK-1.1 condensates appear after 10 minutes of transient hypoxia and disperse after an additional five minutes of normoxia. Values

were normalized to the initial maximum fluorescence value prior to transient hypoxia treatment. The normalized maximum fluorescence values showed significant increases by 1.79 +/- 0.12 fold (normalized mean fold +/- SEM; N=12 condensates) after transient hypoxia, and return to the basal level of 1.00 +/- 0.06 fold (normalized mean fold +/- SEM; N=12 condensates) after five minutes of normoxia. Right panels: image of the neurite prior to transient hypoxia treatment (top, labeled “Initial”), after condensate formation upon ten minutes of transient hypoxia (middle, labeled “10 min hyp”, with condensate pointed out by arrowhead), and upon five minutes of normoxia (lower, labeled “5 min norm”) corresponding to a representative condensate (in magenta) on the graph. Scale, 1 μm.

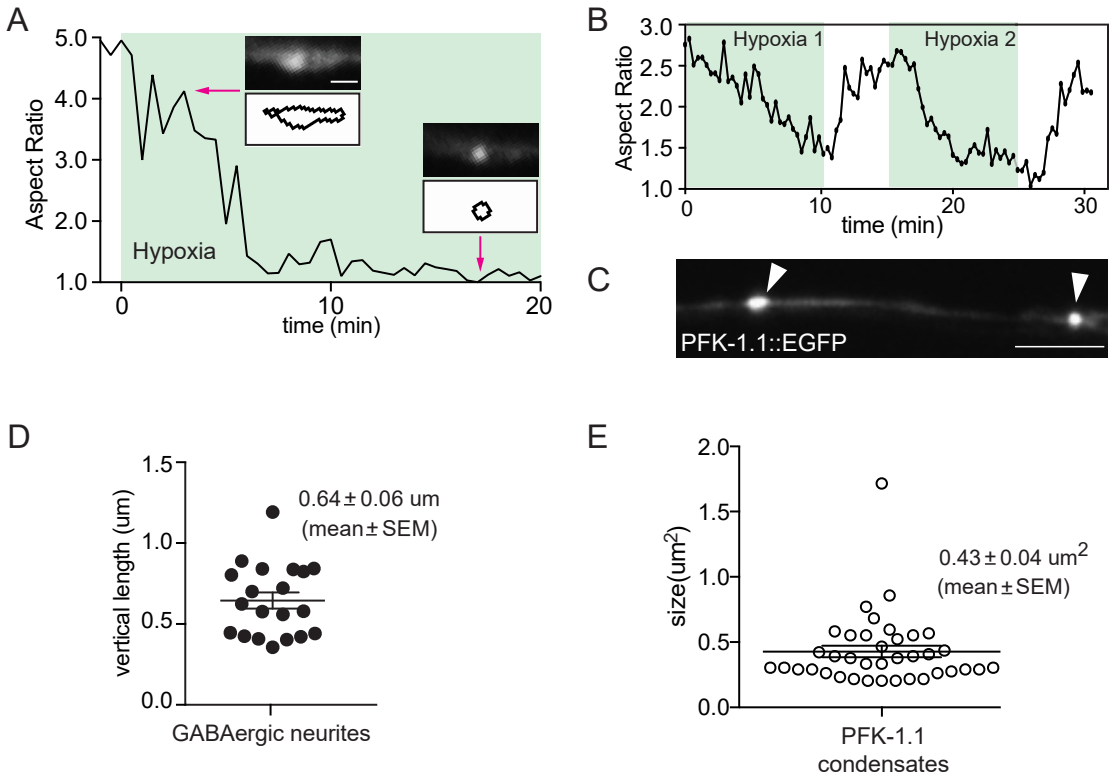

Figure S4. Aspect ratio of PFK-1.1 condensates. (**A**) Changes in the aspect ratio of PFK-1.1 for a given condensate over time. Once transient hypoxia was initiated (green region), the PFK-1.1 coalesced into a spherical structure. Two representative images (left: 3 minutes post-onset of transient hypoxia; right: 17.5 minutes post-onset of transient hypoxia) and corresponding outline of their morphology (white outlined boxes below) used to calculate the aspect ratio. Scale, 2 μm. (**B**) Changes in the aspect ratio of the PFK-1.1 condensates corresponding to Fig. 3 F over time. (**C**) Bigger PFK-1.1 condensates (left arrowhead) look like spherocylinders, as compared to smaller condensates (right arrowhead), which are spherical, suggesting that neurite space may constrain the shape of the fluid condensates. Scale, 5 μm. (**D**) We measured the diameter of GABAergic neurites, as visualized with cytoplasmic mCherry (also measured from electron micrographs, data not shown). Mean vertical length was 0.64 μm (N=20 neurite regions), which would only allow a perfect sphere with a volume of 0.14 μm^3 to fit. (**E**) Measurement of PFK-1.1 condensate size shows an average area of 0.43 +/- 0.04 μm^2 (mean +/- SEM; N=38 condensates) Assuming radial symmetry, its volume would be 0.21 μm^3.

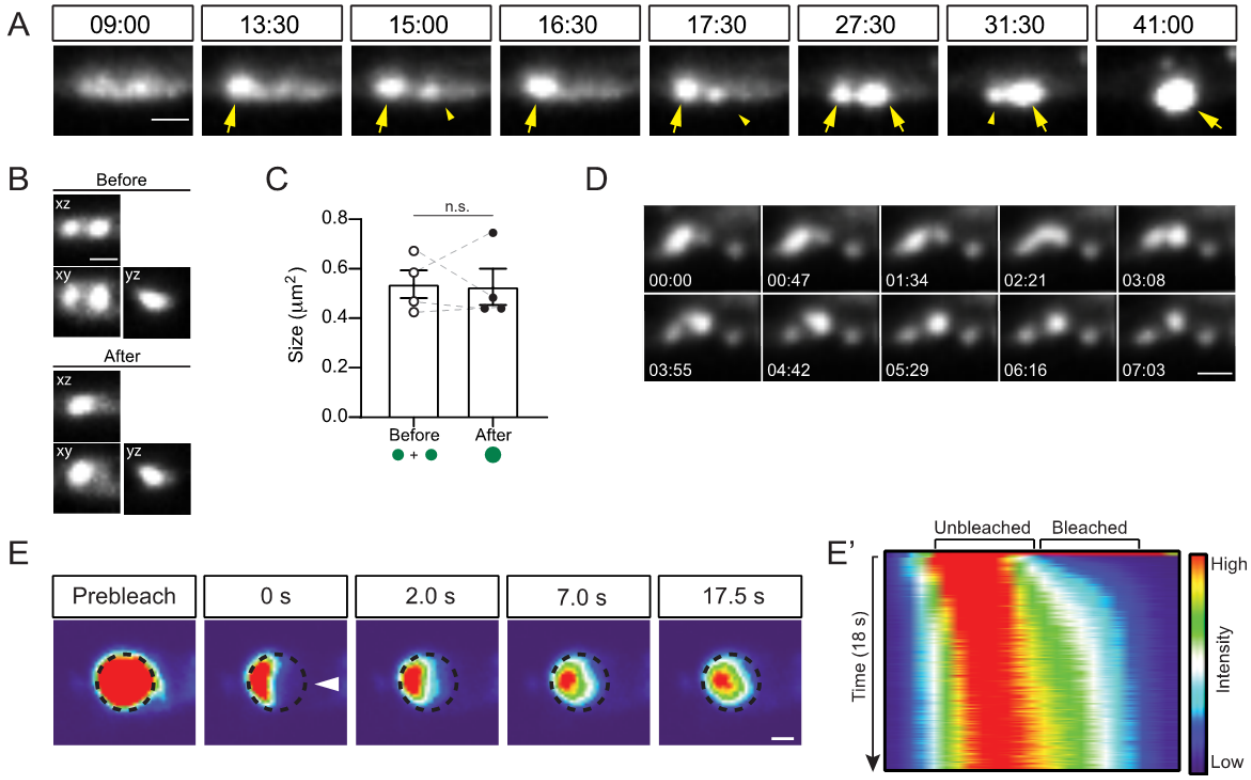

Figure S5. Liquid-like properties of PFK-1.1 condensates. (**A**) Fluid dynamics of two neighboring PFK-1.1 condensates (yellow arrows) upon transient hypoxia (minutes:seconds after induction of transient hypoxia specified on top of the images). The first PFK-1.1 condensate appears in the second montage (13:30) and the second condensate appears soon after (third montage, 15:00). The fluorescence intensity between the two condensates fluctuates until around 32 minutes post hypoxia, which then ends with a fusion event between the two. See also Video S5. Scale, 1 µm. (**B**) Max projection from three different planes (xy, yz, and xz) before fusion and after fusion of Fig. 4 C from three projections (xz, xy and yz) demonstrating fusion. (**C**) Quantification of four separate fusion events (each connected by dotted gray lines). When the total area of PFK-1.1 condensates is measured before fusion (open circles), and after fusion (black circle), no significant difference is observed. (**D**) Additional timeframes for Fig. 4 D. Elapsed time from the beginning of the imaging session is indicated for each image in

minutes:seconds. Scale, 1 μm. (**E-E'**) Fluorescence recovery after photobleaching of a PFK-1.1 condensate in the cell body of a neuron also shows similar recovery dynamics to those observed in the neurites (compare with Fig. 5 A). PFK-1.1::EGFP condensate initial shape outlined with dashed circle, and partial area bleached highlighted with arrowhead in second panel. Scale, 1 μm. In C', kymograph of the partially bleached condensate and recovery dynamics.

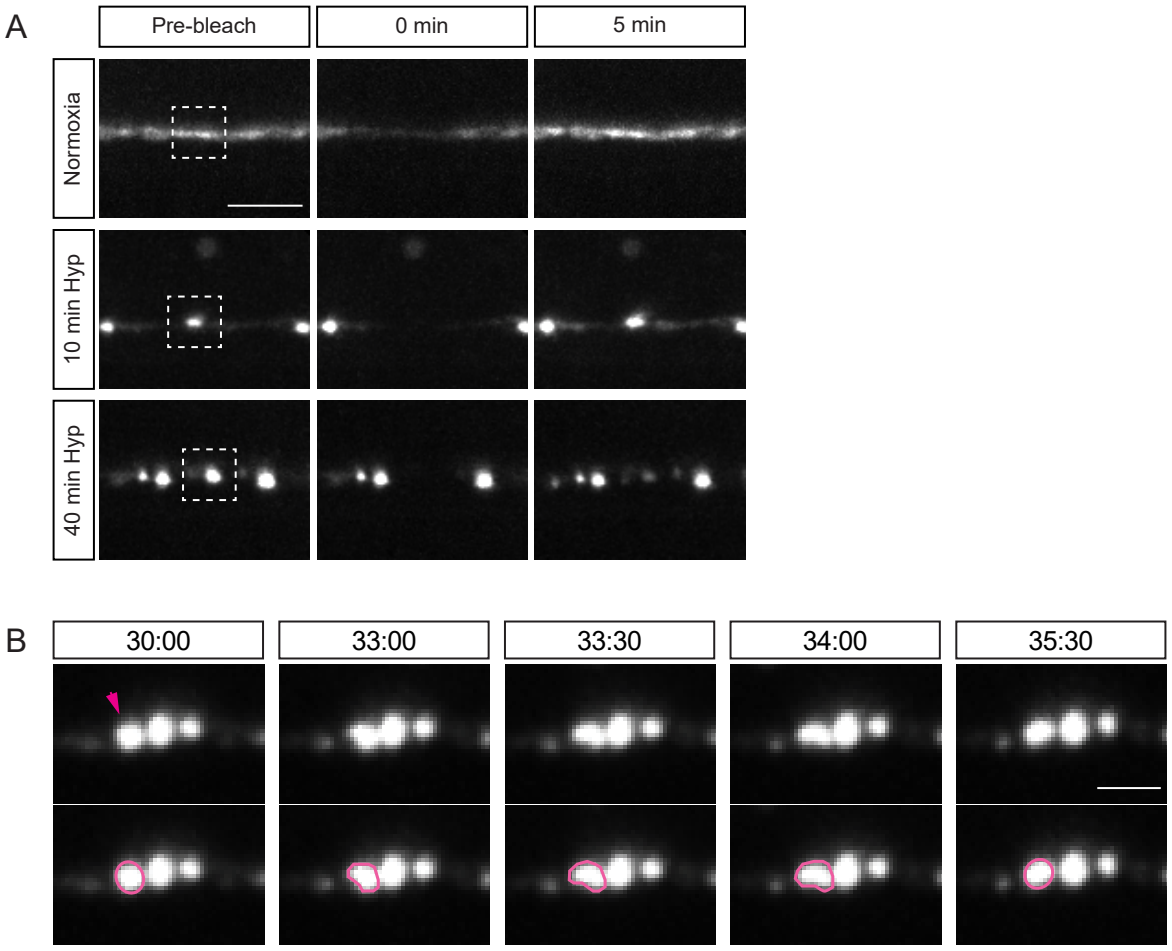

Figure S6. Changes in PFK-1.1 condensate properties. (**A**) Complete photobleaching of PFK-1.1 condensates, and fluorescence recovery. Dashed box indicates the photo-bleached area. Before photobleaching (Pre-bleach), at the time of photobleaching (0 min) and post 5 minutes of photobleaching are shown for PFK-1.1 under three conditions: normoxia, after 10 minutes of hypoxia and 40 minutes of hypoxia. We note that besides the proposed changes in the material properties of the condensates, there could also be a corresponding deeper quench of the cytoplasmic PFK-1.1 material, resulting in a concomitant lower protein concentration in the dilute phase during the hardening of the condensates from prolongued hypoxia. Scale, 5 µm. (**B**) A PFK-1.1 condensate displays fluid motions (magenta arrowhead and outline in lower panels) as it bounces away from its closely neighboring condensates. Time elapsed since the

start of transient hypoxia is indicated above in minutes:seconds. See also Video S6. Scale, 2 µm.

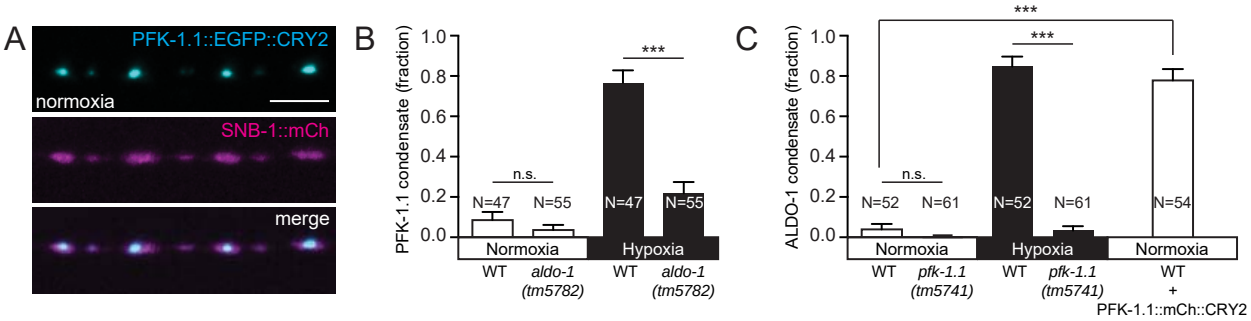

Figure S7. PFK-1.1 and ALDO-1 condensates

(**A**) PFK-1.1::EGFP::CRY2 (cyan) forms clusters near synapses (as visualized with SNB-1/synaptobrevin (magenta) in GABAergic neuron) even in normoxic conditions, indicating the ability of CRY2 to promote condensate formation. Scale, 5 µm. (**B**) Fraction of animals that display PFK-1.1::EGFP condensates for in wild-type (WT) or *aldo-1 (tm5782)* mutant backgrounds (from Fig. 7 F). (**C**) Fraction of animals that display ALDO-1::EGFP condensates in in wild-type (WT) or *pfk-1.1 (tm5741)* mutant background (from Fig. 7 G) or ALDO-1::EGFP co-expressed with PFK-1.1::mCh::CRY2 (from Fig. 7 H). N indicates the number of animals scored. Error bars denote SEM. *, $p < 0.05$. **, $p < 0.01$. ***, $p < 0.001$ between indicated group.

Supporting References

1. Dickinson, D.J., A.M. Pani, J.K. Heppert, C.D. Higgins, and B. Goldstein. 2015. Streamlined Genome Engineering with a Self-Excising Drug Selection Cassette. *Genetics*. 200:1035–1049.

2. Schwartz, M.L., and E.M. Jorgensen. 2016. SapTrap, a Toolkit for High-Throughput CRISPR/Cas9 Gene Modification in Caenorhabditis elegans. *Genetics*. 202:1277–1288.

3. Mello, C., and A. Fire. 1995. DNA transformation. *Methods Cell Biol*. 48:451–82.

4. Lagoy, R.C., and D.R. Albrecht. 2015. Microfluidic Devices for Behavioral Analysis, Microscopy, and Neuronal Imaging in Caenorhabditis elegans. *Methods Mol Biol*. 1327:159–79.

5. Burnett, K., E. Edsinger, and D.R. Albrecht. 2018. Rapid and gentle hydrogel encapsulation of living organisms enables long-term microscopy over multiple hours. *Commun. Biol.* 1:73.

6. Powell-Coffman, J.A. 2010. Hypoxia signaling and resistance in C. elegans. *Trends Endocrinol. Metab. TEM*. 21:435–440.

7. Thévenaz, P., U.E. Ruttimann, and M. Unser. 1998. A pyramid approach to subpixel registration based on intensity. *IEEE Trans. Image Process. Publ. IEEE Signal Process. Soc.* 7:27–41.

8. Jang, S., J.C. Nelson, E.G. Bend, L. Rodriguez-Laureano, F.G. Tueros, L. Cartagenova, K. Underwood, E.M. Jorgensen, and D.A. Colon-Ramos. 2016. Glycolytic Enzymes Localize to Synapses under Energy Stress to Support Synaptic Function. *Neuron*. 90:278–91.

9. Huelgas-Morales, G., C.G. Silva-García, L.S. Salinas, D. Greenstein, and R.E. Navarro. 2016. The Stress Granule RNA-Binding Protein TIAR-1 Protects Female Germ Cells from Heat Shock in Caenorhabditis elegans. *G3 Bethesda Md*. 6:1031–1047.

10. Sun, Y., P. Yang, Y. Zhang, X. Bao, J. Li, W. Hou, X. Yao, J. Han, and H. Zhang. 2011. A genome-wide RNAi screen identifies genes regulating the formation of P bodies in C. elegans and their functions in NMD and RNAi. *Protein Cell*. 2:918–939.

11. Xuan, Z., L. Manning, J. Nelson, J.E. Richmond, D.A. Colon-Ramos, K. Shen, and P.T. Kurshan. 2017. Clarinet (CLA-1), a novel active zone protein required for synaptic vesicle clustering and release. *Elife*. 6.